Quiet periods in edge turbulence preceding the L-H transition in the National Spherical Torus Experiment

S. J. Zweben,[1] R. J. Maqueda,[1] R. Hager,[2] K. Hallatschek,[2] S. M. Kaye,[1] T. Munsat,[3]
F. M. Poli,[4] A. L. Roquemore,[1] Y. Sechrest,[3] and D. P. Stotler[1]

[1]*Princeton Plasma Physics Laboratory, Princeton, New Jersey 08540, USA*
[2]*Max-Planck-Institut für Plasmaphysik, Boltzmannstraße 2, D-85748 Garching, Germany*
[3]*University of Colorado, Boulder, Colorado 80309, USA*
[4]*University of Warwick, Coventry CV4 7AL, United Kingdom*

This paper describes the first observations in the National Spherical Torus Experiment (NSTX) [S. M. Kaye *et al.*, Phys. Plasmas **8**, 1977 (2001)] of "quiet periods" in the edge turbulence preceding the low-to-high (L-H) mode transition, as diagnosed by the gas puff imaging (GPI) diagnostic near the outer midplane separatrix. During these quiet periods the GPI D_α light emission pattern was transiently similar to that seen during H-mode, i.e., with a relatively small fraction of the GPI light emission located outside the separatrix. These quiet periods had a frequency of ~ 3 kHz for at least 30 ms before the L-H transition, and were correlated with changes in the direction of the local poloidal velocity. The GPI turbulence images were also analyzed to obtain an estimate for the dimensionless poloidal shearing $S = (dV_p/dr)(L_r/L_p)\tau$. The values of S were strongly modulated by the quiet periods but did not significantly vary during the ~ 30 ms preceding the L-H transition. Since neither the quiet periods nor the shear flow increased immediately preceding the L-H transition, neither of these appears to be the trigger for this transition, at least for these cases in NSTX. © *2010 American Institute of Physics*. [doi:10.1063/1.3476276]

I. INTRODUCTION

This paper describes experimental observations of H-mode-like "quiet periods" in edge turbulence which precede the main low-to-high (L-H) mode transition in the National Spherical Torus Experiment (NSTX), a low aspect ratio tokamak.[1] These quiet periods occur with a frequency of ~ 3 kHz for at least 30 ms before transition, and are well correlated with local reversals in the poloidal flow speed of the edge turbulence. These observations are similar to previous results on edge zonal flows in tokamaks and similar devices, but do not yet identify a "trigger" mechanism for the main L-H transition.

The subject of L-H transitions in tokamaks has been an area of intense research for over 25 years, as discussed in detail in review articles about both experiments[2] and theory.[3] There is clear experimental evidence for a fast reduction in the level of edge turbulence at the L-H transition, e.g., Refs. 4–6, and for an increase in the edge radial electric field and poloidal flow across transition in space and time, e.g., Refs. 6 and 7. However, since the transition occurs rapidly and nearly simultaneously with the changes in edge turbulence and radial electric fields, it has been difficult to identify the causal relationship between these phenomena or to find a trigger mechanism for the L-H transition, as discussed in several previous reviews.[8–11] For example, there was some evidence for a change in the poloidal rotation and radial electric field of ~ 1 ms before the transition in DIII-D,[5] but no evidence of a poloidal spin-up prior to the L-H transition has been observed in JET (with a time resolution of 50 ms).[12]

There have been many theoretical models for the L-H transition, as reviewed in Ref. 3. The earliest analytic theories attributed the transition to changes in the radial electric field and its associated poloidal ExB drift, either due to nonambipolar ion orbit loss,[13] neoclassical viscosity,[14] spontaneous poloidal spin-up,[15] or edge turbulence suppression.[16] The most recent analytic theories of the L-H transition emphasize the complexity of bifurcation physics[17] and consider the influence of geodesic acoustic modes (GAMs).[18] The complexities can in principle be resolved through numerical simulations of edge turbulence and transport, which have in some cases seemed to reproduce the L-H transition.[19–21] Yet in practical terms, neither analytic theory nor simulation is presently being used to predict the power needed to produce an L-H transition in ITER, so there is clearly a need for improved understanding in this area.

A recent and important development in the field of tokamak edge turbulence and transport has been the theory[22] and experimental observations[23] of zonal flows, which are localized poloidal flows with a low but finite real frequency. Clear experimental evidence for GAMs, which are coherent zonal flows, has been obtained in the edge region of several fusion devices using several different diagnostics.[24–33] These GAMs are observed just inside the separatrix and have a frequency which scales with the sound speed and major radius, i.e., $\omega \sim c_s/R$. There is also experimental evidence for lower-frequency incoherent zonal flows in the edge region, e.g., in DIII-D[30] and ASDEX-Upgrade.[31] An energy exchange between GAMs, lower frequency zonal flows, mean ExB flows, and the level of turbulence has been measured in JFT-2M,[6] the H-1 Heliac,[32] and HL-2A tokamaks.[33] These and many other results concerning the interactions between zonal flows

and turbulence are discussed in two comprehensive review papers.[22,23]

Given this background on L-H transitions and zonal flows, we now review some previous measurements specifically concerning changes in the edge turbulence and poloidal flows preceding the L-H transition, which is the subject of the present paper. The first detailed study of edge fluctuations at the L-H transition was made using Langmuir probes in PBX-M.[34] In that experiment the fluctuation levels and turbulent transport were significantly reduced at the transition, but there was only a modest increase in the velocity shear, and the changes in turbulent transport were not confined to the region of large velocity shear. Subsequent edge probe measurements in HT-6M provided evidence for a link between turbulent flows driven by Reynolds stress and the onset of improved Ohmic confinement.[35] Edge measurements made using a heavy ion beam probe on JFT-2M showed that the edge fluctuations and edge potential changed at the same time at the L-H transition to within 128 μs.[6] Edge measurements made using correlation reflectometry at the L-H transition in W7-AS[36] showed a large and often correlated oscillation in poloidal flow and density fluctuations before the transition, with a single step in density fluctuations without any change in poloidal flow at the main transition. A similar reflectometry measurement in the TJ-II stellarator showed that the edge turbulence reduction at the transition was coincident with an increase in the low frequency oscillating sheared flow, but preceded the increase in the mean shear flow.[37] Measurements of poloidal edge flows made using beam emission spectroscopy (BES) in DIII-D showed that GAMs disappeared well before the L-H transition, but the relatively larger and lower-frequency "zero mean frequency zonal flow" appeared ~70 ms preceding the L-H transition, along with an increase in mean flow and flow shear.[30] These measurements were averaged over 50 ms so their exact relationship to the rapid (<100 μs) drop in fluctuation level at the transition was not determined.

Previous measurements made using gas puff imaging (GPI) in NSTX showed a clear reduction in turbulence at the L-H transition,[38] with little or no change in correlation lengths or poloidal flow speeds before and after the L-H transition. However, those measurements only had 300 frames/shot (1.2 ms) so they could only capture a few transitions and were of limited use for studying changes preceding the transition. Additional fast photomultiplier tube detector radial arrays were also used to examine the bicoherence just prior to the transition,[39] but those were limited to 13 spatial channels.

In summary, many good measurements have been made concerning the interaction between edge turbulence, edge flows, and L-H transitions, and interesting connections have been made between those measurements and the theory of edge turbulence and zonal flows. Yet the exact mechanism for the trigger of the transition has not yet been identified.[2,10] Therefore the goal of the present paper is to evaluate the two-dimensional (2-D) edge turbulence characteristics and poloidal flow shear preceding the L-H transition in NSTX. The data were acquired using an upgraded version of the GPI diagnostic on NSTX, as discussed in Sec. II. Section III describes the observations of quiet periods preceding the L-H transition, Sec. IV discusses the turbulence shear flows, Sec. V describes the larger database, and Sec. VI contains the discussion.

II. UPGRADED GPI DIAGNOSTIC IN NSTX

The present paper describes recent L-H transition measurements made in NSTX using an improved fast camera system which can record 2-D turbulence images at ≤285 000 frames/s at a resolution of 64×64 pixels for up to 50 ms. This upgraded hardware allowed 2-D images of the L-H transition to be captured for many shots, which was not possible previously.

The basic GPI diagnostic on NSTX (R_o=85 cm, a=65 cm) has been described in detail elsewhere.[40,41] For the present paper the turbulent fluctuations are measured by the excitation of the visible D_α (656 nm) line emission from a deuterium gas puff. Since the turbulence is highly elongated along the magnetic field B, the visible light from the GPI gas puff cloud was viewed along the local B field (to within a few degrees) to resolve the radial versus poloidal structure of the turbulence. The GPI gas cloud increases the brightness of the D_α by $\sim \times 20$ above the background, and thus localizes the emission for improved spatial resolution.

Figure 1(a) shows a schematic view of the GPI diagnostic geometry in NSTX, including a turbulence filament aligned along B and its intersection with the GPI gas cloud ("blob"). Figure 1(b) shows the location of the GPI field of view, which is centered ~20 cm above the outer midplane near the separatrix, and extends ~25 cm radially and ~25 cm poloidally. The spatial resolution of the optics is ~0.3 cm and the spatial resolution set by the curvature of the field lines within the GPI gas cloud is ≤1 cm. This is small enough to resolve the edge turbulence structures in NSTX, which have a typical correlation length of ~3–5 cm.

To get the highest possible framing rate for this experiment, two Phantom 7.3 cameras viewed the same GPI image using a beam splitter, and their recording times were interlaced. This allowed a framing rate of up to 285 000 frames/s (3.5 μs/frame) with an exposure time of 3 μs/frame at 64×64 pixel resolution. This is only slightly higher than the 250 000 frames/s rate of the Princeton Scientific Instruments PSI-5 camera used previously,[40] but these Phantom cameras allow the capture of typically 17 000 frames/shot, whereas the PSI-5 camera allowed only 300 frames/shot. Therefore at the highest framing rate the present cameras recorded ~50 ms/shot, which made it relatively easy to capture L-H transitions.

Typical single images from the camera are shown in Fig. 2 for L-mode (top) and H-mode (bottom), both taken with an exposure time of 3 μs. These images are oriented with the local minor radial direction approximately horizontal (outward to the right) and the local poloidal direction (within a magnetic flux surface) approximately vertical, with the ion diamagnetic and grad-B drift direction downward. The GPI light intensity is shown in a linear false color scale, the location of the separatrix (according to the NSTX equilibrium
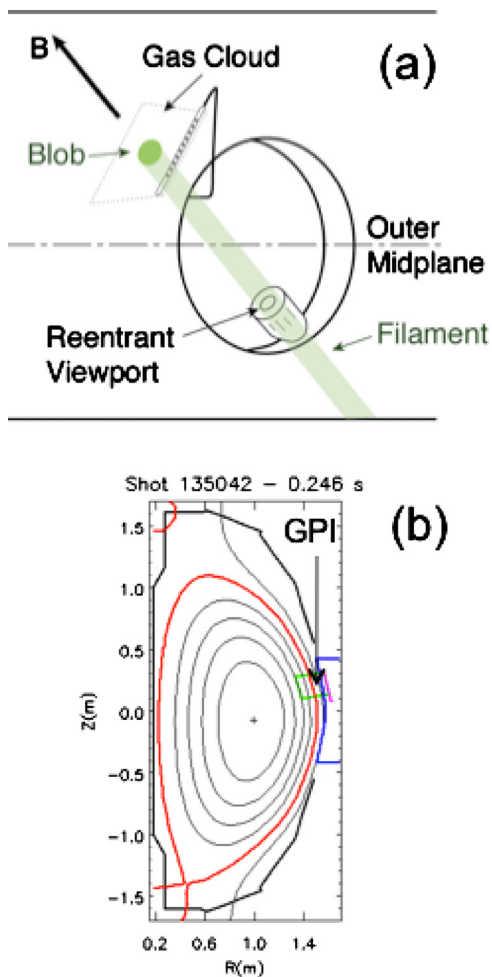
FIG. 1. (Color online) Geometry of the GPI diagnostic in NSTX. In (a) is a sketch of the vessel outer wall (as seen from the plasma) showing the reentrant GPI viewport, the manifold from which the gas puff emerges, and the approximate angle of the local magnetic field. The 3-D structure of the turbulence is shown as a "filament," and the 2-D projection of a filament with the GPI radial vs poloidal plane is shown as a "blob." In (b) is an equilibrium at the L-H transition time for #135042, along with the GPI area projected into the (R, z) plane, the location of the GPI manifold (the line just outside the GPI area), and the projection of the rf antenna/limiter in this plane (covering far right around the midplane).

FIG. 2. (Color) Typical GPI images of the D_α light emission in this experiment. At the top is an L-mode image and at the bottom is an H-mode image later in the same shot, both images taken with 3 μs exposure times and the same (false) color intensity scale. Also shown is the best estimate for the separatrix location (dashed line) and the shadow of the rf antenna/limiter location (dotted line). These images cover a region of ~25 cm in the radial (horizontal) direction and ~25 cm in the poloidal (vertical) direction, and have a pixel size of ~0.4 cm. The range of GPI turbulence analysis is shown by the rectangle in the middle.

code) is shown by the dashed line, and the location of the shadow of the nearest limiter (rf antenna) is shown by the dotted line to the right. The GPI gas manifold is located just outside the limiter shadow. The GPI light (D_α emission) in L-mode shows a complex turbulent pattern which extends up to ~5 cm into the scrape-off layer (SOL) outside the separatrix, while in H-mode the GPI light shows a quiescent poloidal band just inside the separatrix. The box in the center of Fig. 2 shows the radial and poloidal range used for GPI data analysis (± 4 cm around the separatrix), although much of the analysis is done in the middle of this box near the separatrix.

The interpretation of the GPI images has also been described previously.[40–42] The D_α light emission is located in the region where the neutrals are excited but not yet ionized, which corresponds roughly to $T_e \approx 5 - 100$ eV. Within this temperature range the line emission at a given neutral density is a nonlinear (but monotonically increasing) function of the
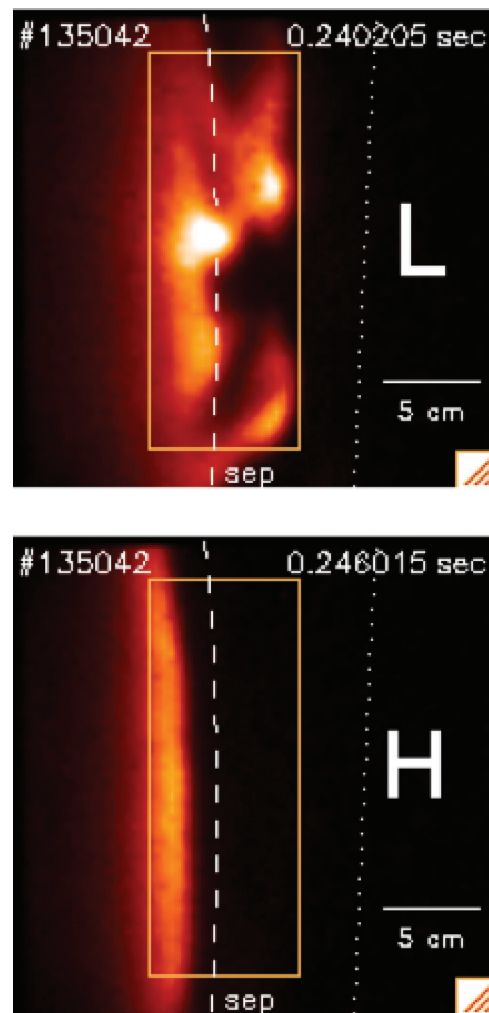
local electron density n_e and electron temperature T_e, while the neutral deuterium density is monotonically decreasing toward the plasma center. The radial profiles of D_α light are consistent with DEGAS 2 calculations based on the measured profiles and neutral gas transport from the gas manifold.[42]

Although the GPI light emission is a nonlinear function of the local density and temperature, the structure and motion of the GPI light fluctuations, as determined by the space-time cross-correlation functions, are nearly independent of the details of this nonlinearity, as discussed previously.[40] This effect is similar to a television image in which the structure and motion of an object are independent of the nonlinearity controlled by the contrast setting. Thus the turbulence correlation lengths, times, and speeds can be calculated directly from the GPI data. However, the GPI diagnostic is not able to measure either the absolute or relative density fluc-

TABLE I. L-H transition database of fast GPI data.

Shot	I (MA)	B (kG)	L-H time (s)	GPI data (s)	NBI (MW)	Time/frame (μs)
132682	0.8	4.4	0.2544	0.170–0.252	1.9–3.0	8.25
132712	0.8	4.5	0.3375	0.200–0.282	0.9–2.4	8.25
132716	0.8	4.5	$\cdots$	0.200–0.250	0	8.25
132719	0.8	4.3	$\cdots$	0.200–0.250	1.7–2.3	8.25
132959	0.92	4.4	0.2525	0.220–0.260	1.2	6.75
132967	0.92	4.4	0.2555	0.220–0.260	2.8	6.75
135020	0.8	4.5	0.1750	0.205–0.260	0.8–2.7	7.0
135021	0.9	4.5	0.2391	0.205–0.260	0.8–2.7	3.5
135022	0.92	4.5	0.2507	0.215–0.260	0.8–2.6	3.5
135023	0.92	4.5	0.2518	0.215–0.260	0.8–4.5	3.5
135041	0.92	4.5	0.2495	0.215–0.275	0.7–2.6	3.5
135042	0.92	4.5	0.2455	0.215–0.275	0.7–2.6	3.5
135043	0.92	4.5	0.2500	0.215–0.275	0.7–2.6	3.5
135044	0.92	4.5	0.2451	0.215–0.275	0.7–2.6	3.5
135045	0.92	4.5	0.2435	0.215–0.275	0.7–2.6	3.5
135046	0.92	4.5	0.2539	0.225–0.275	0.7–2.6	3.5

tuation level, since the observed D_α emission is a function of both density and temperature, and neither of these is independently measured on the relevant fast timescale.

III. QUIET PERIODS

GPI data were acquired and analyzed for the NSTX discharges and plasma conditions listed in Table I. These discharges were standard neutral beam injection (NBI)-heated plasmas with $B \sim 4.5$ kG, $I \sim 0.8-0.9$ MA in a lower single null configuration with the ion grad-B drift toward the X-point. The H-mode transitions typically occurred just after an increase in the NBI power from 0.7 to 2.5 MW. This data set includes nine shots with an L-H transition captured at the highest available frame rate of (3.5 μs/frame), four shots with L-H transitions captured at a slower frame rate, two shots in L-mode only, and one shot in H-mode only. Most of the analysis in Secs. III and IV is done for three typical shots in this list (#135042–135044), which had identical external parameters. The larger database is discussed in Sec. V.

Figure 3 shows the time dependence of D_α light emission from the GPI diagnostic within an ~ 1.5 cm wide region radially centered at $\rho = 0.4$ cm (with respect to the separatrix) and ~ 20 cm high in the poloidal direction (see box in Fig. 2). The GPI signal from this region dropped rapidly at the H-mode transition at ~ 0.2454 s, at about the same time as the (slower) D_α light emission far away from the GPI (below). At the right of Fig. 3 are the Thomson scattering profiles just before and just after the H-mode transition in this shot (#135042), showing the formation of a strong density "transport barrier" in the edge density near the separatrix (labeled "sep."). The times of this Thomson scattering data are shown at the bottom left; thus this barrier was formed ≤ 3 ms after the transition. The radial range of the GPI di-

agnostic with respect to the outer midplane flux surfaces is indicated by the arrows at the right in Fig. 3; the GPI viewing region extends radially from ~ 10 cm inside to ~ 15 cm outside the separatrix. The edge barrier in these cases is formed in the electron density and not the electron temperature, and the top of the barrier pedestal in H-mode is just inside the peak of the GPI light emission in Fig. 2.

Figure 4 shows the time dependence of the GPI signals during an ~ 10 ms period near the L-H transition (vertical line) for three shots for the same spatial region as Fig. 3, i.e., within an ~ 1.5 cm wide region radially centered at $\rho = 0.4$ cm. In each of these shots there appears to be a series of transient "quiet" periods of low GPI signal level preceding the transition, several of which are circled. These quiet periods have a GPI signal level in this region nearly as low as that during the quietest time of the H-mode period of ≤ 2 ms after the transition. These quiet periods also appear earlier in the L-mode phase, as discussed in Sec. V. Later in the H-mode phase the GPI signals show stronger intermittent bursts, which will not be discussed in this paper.

Figure 5 shows the sequence of GPI images for a typical ~ 250 μs period near one of the quiet times circled in Fig. 4 (#135044 at 0.237 225–0.237 435 s). Each frame has an exposure time of 3 μs, the time between frames is 3.5 μs, and the approximate location of the separatrix is shown by the vertical line in each frame. The quiet period labeled "Q" in Fig. 5 lasts for 16 frames (60 μs). During this period the GPI images look more similar to those during H-mode than to L-mode (see Fig. 2), i.e., with a narrow radial profile of D_α emission just inside the separatrix, along with a lower radial correlation length of the turbulence, as discussed below and in Sec. IV.

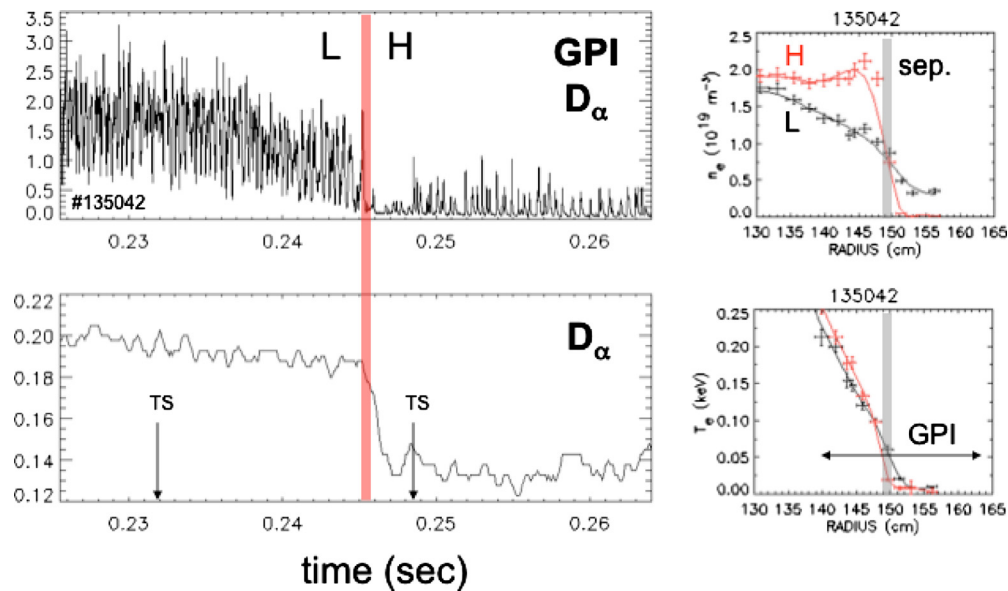Therefore an empirical way to characterize the "H-

FIG. 3. (Color online) Time dependence of D_α light emission from the GPI diagnostic within a 1.5 cm wide region just outside the separatrix at $\rho = 0.4$ cm. This GPI signal drops rapidly at the H-mode transition at ~0.2454 s, at about the same time as the standard D_α light emission far from the GPI puff (the latter has a slower response time). At the right are Thomson scattering profiles just before and just after the H-mode transition showing the formation of an edge density transport barrier after the transition. The times of these Thomson scattering data are shown at the bottom left. The radial range of the GPI diagnostic with respect to the outer midplane flux surfaces is also shown at the right, along with the separatrix location (labeled sep.).
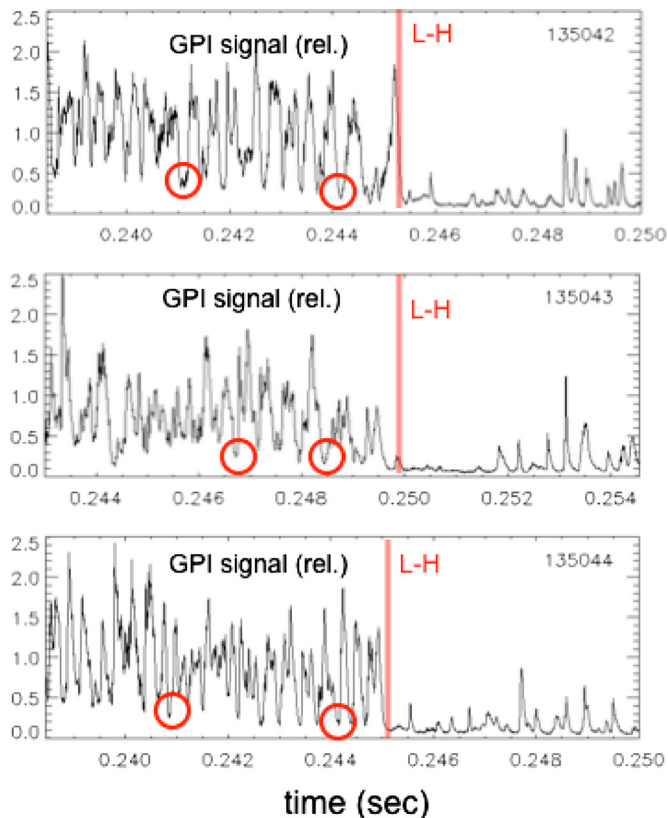

FIG. 4. (Color online) Time dependence of the GPI signal during an ~10 ms time period around the L-H transition for the same spatial region, i.e., just outside the separatrix for the same spatial region as Fig. 3. Three successive shots are shown which were taken under identical machine conditions. In each of these shots there are many transient quiet periods preceding the transition, which have a GPI signal level similar to the period ≤2 ms after the L-H transition.

mode-ness" of the GPI data is to calculate the fraction of the GPI light emission located radially outside the separatrix "F_{sol}". This parameter is an indirect measure of fast changes in the radial density and temperature profiles near the separatrix which cause these changes in the profile of D_α (such fast ~10–100 μs changes in edge profiles are not measured by any other NSTX diagnostic). This F_{sol} fraction is shown in Fig. 6 over a longer period of time around the L-H transition for the same three shots as for Fig. 5. The lines versus time are this fraction smoothed over 0.7 ms (200 frames), and the dashed line at 0.15 is just shown as a reference. In all cases the F_{sol} drops rapidly at the transition (vertical lines), corresponding to the change in the emission profiles illustrated in Fig. 2. The quiet periods with $F_{sol} < 0.20$ can be seen to occur for at least 20 ms before the transition.

To further clarify the nature of the quiet periods, Fig. 7(a) plots the radial profiles of the images during the L-mode period in Fig. 4 for #135042, sorted according to their SOL fraction F_{sol}. The curve labeled "mean L-mode" includes all the images in the L-mode time period (0.238 455–0.245 105 s), and the curve labeled "mean H-mode" includes all images in the H-mode period just after the transition when F_{sol} is lowest (0.245 445–0.248 340 s). The other curves include only images in L-mode with signal levels below $F_{sol} = 0.15$, 0.2, or 0.4. The quietest periods in L-mode have radial D_α profiles which look like those seen just after the L-H transition. Figure 7(b) shows the radial profile of the relative GPI rms fluctuation level (normalized to its mean) versus F_{sol} for the same data. The relative GPI fluctuation level profiles of the quiet periods in L-mode are also similar to those in H-mode, i.e., with a lower relative fluctuation level in the SOL. Similar results are obtained for shots 135043 and 135044.

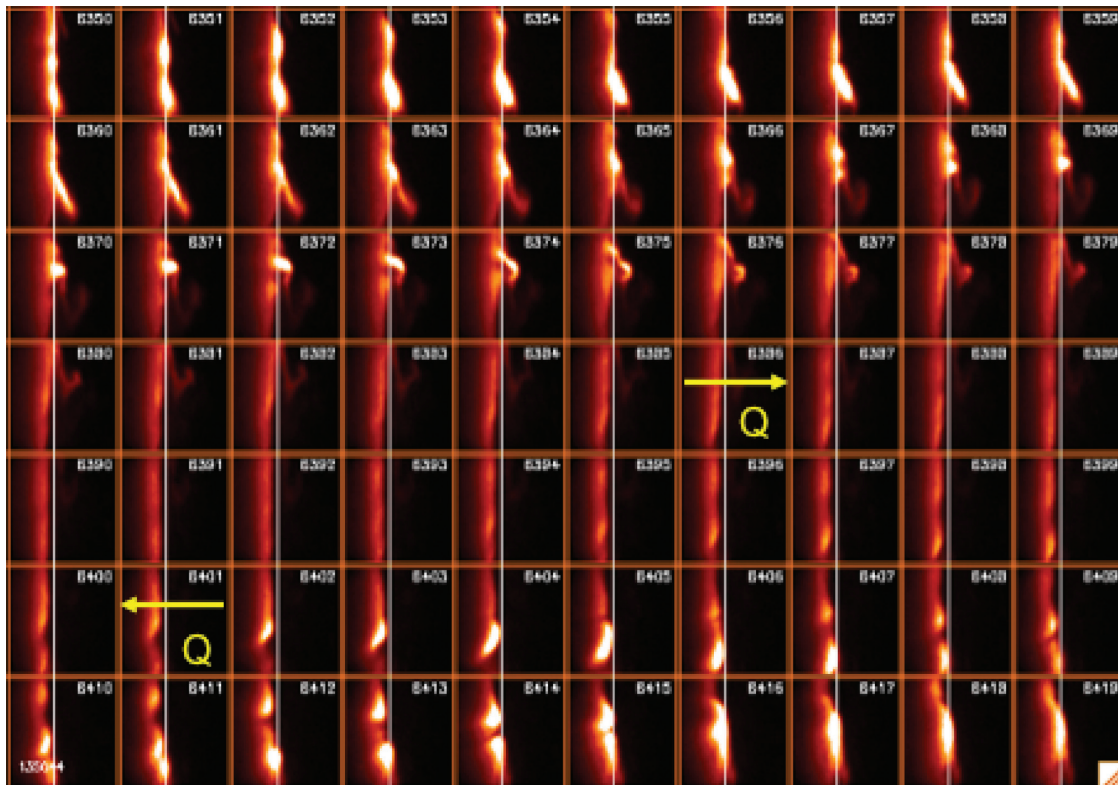Figure 8 shows the time dynamics of the radial and po-

FIG. 5. (Color) Sequence of GPI images for an ~ 250 μs (70 frames) period showing a typical quiet time (#135044 at 0.237 225–0.237 435 s). Each frame has an exposure time of 3 μs, and the approximate location of the separatrix is shown by the vertical line in each frame. This quiet period (labeled "Q") lasts for ~ 16 frames, i.e., 60 μs. During this time the GPI images look like those seen in H-mode rather than those usually seen in L-mode (see Fig. 2). (enhanced online). [URL: http://dx.doi.org/10.1063/1.3476276.1] [URL: http://dx.doi.org/10.1063/1.3476276.2] [URL: http://dx.doi.org/10.1063/1.3476276.3]

loidal profiles of the GPI data for a time between ~ 2 ms before to ~ 0.5 ms after the L-H transition for shot 135044. Part (a) shows the time dependence of the GPI light versus radius within a row of pixels at the vertical center of the images, part (b) shows the time dependence of the GPI light versus poloidal distance in a column of pixels near the separatrix at $\rho \sim 0$, and part (c) shows the time dependence of the GPI light versus poloidal distance in a column of pixels well inside the separatrix at $\rho \sim -3$ cm near where the GPI light peaks during H-mode. The corresponding F_{sol} levels are shown by the bands at the right, where white is $F_{sol}=1$ and black is $F_{sol}=0$. The quiet periods are labeled with Q, the H-mode period is labeled as H, the transition is shown as a horizontal dashed line, and the separatrix is shown as a vertical dashed line in (a).

In Fig. 8 there are five H-mode-like quiet periods during the 2 ms preceding the L-H transition, not quite evenly spaced in time. Between each of the quiet periods there are many faster bursts or "blobs" of GPI light extending well into the SOL with a radially outward direction of motion, i.e., tilted downward and to the right in the radial plot in Fig. 8(a). In the poloidal direction the quiet periods near the separatrix in Fig. 8(b) begin at the right-hand side, which corresponds to the top of the images in Fig. 2, and the fast bursts between quiet periods mainly propagate in the ion diamagnetic direction, i.e., downward to the left. But inside the separatrix, as shown in Fig. 8(c), the fast bursts of turbulence during the quiet periods propagate mainly in the electron

diamagnetic direction, i.e., downward to the right. However, transient reversals in the direction of poloidal propagation can also be seen in both Figs. 8(b) and 8(c). Thus the behavior of the edge turbulence is strongly modified during the quiet periods, but these changes vary with radius and time in a complex way, as discussed further in Sec. IV.

The timing of the main H-mode transition itself can be clearly seen in Figs. 8(a) and 8(b), and also in the three cases of Fig. 6, as the beginning of the sudden and sustained drop in the GPI light outside the separatrix. This timing can be estimated from the GPI data to within about ±0.2 ms (the GPI data are presently the best available timing signal for the L-H transition in NSTX). There does not appear to be any conspicuous trigger event for the main transition in the raw data such as Fig. 8, and it is not obvious from these data where the transition begins in radius (or poloidal angle).

To examine the time variation of the quiet periods, Figure 9(a) shows the autocorrelation function of F_{sol} versus delay time for the same three shots as in Fig. 6, averaged over a 10 ms period preceding the L-H transition in each case. The autocorrelation functions all have a quasiperiodic structure with a period of $\sim 300-400$ μs, which is also visible in the raw data of Figs. 5 and 8. Figure 9(b) shows the power spectra of F_{sol} for the same data, which has relatively broad peaks at a frequency of ~ 3 kHz, corresponding to the main oscillations in Fig. 9(a), as expected.

Thus Figs. 5–9 show evidence for quasiperiodic H-mode-like quiet periods in the D_α light emission near the
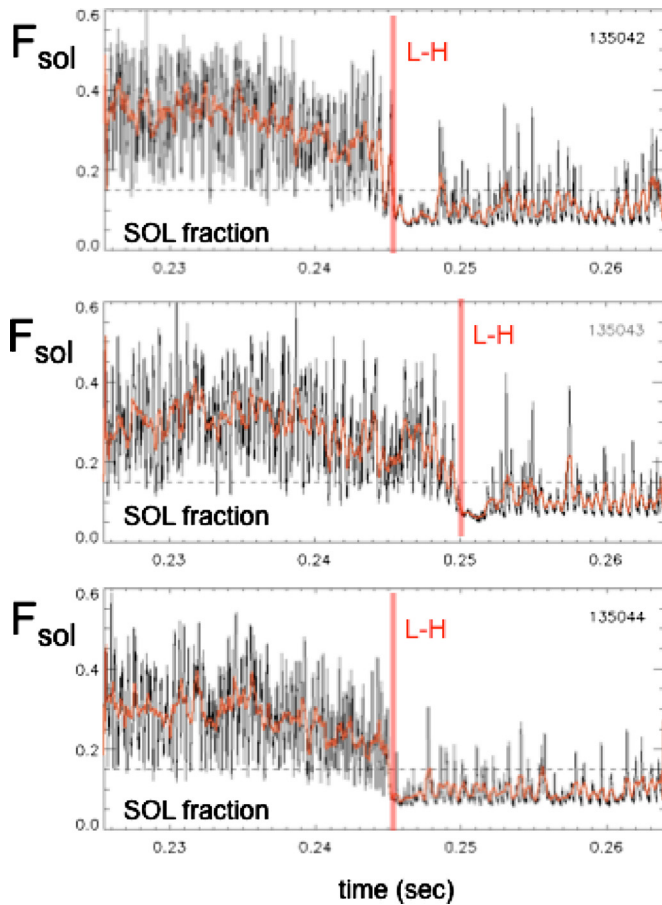
FIG. 6. (Color online) Fraction of the GPI light emission located outside separatrix F_{sol} vs time for the same three shots as for Fig. 4. The lines are this fraction smoothed over 0.7 ms (200 frames), and the dashed line at 0.15 is just shown for reference. In all cases F_{sol} rapidly drops below 0.15 at the L-H transition (vertical line), but occasionally goes below 0.20 before the L-H transition (quiet periods). Well after the main transition, F_{sol} shows intermittent bursts above $F_{sol}=0.15$ for the remainder of the H-mode period.

separatrix at least 10–20 ms preceding the main L-H transition. Section IV describes the connection between these quiet periods and other time-dependent statistical analyses of the GPI data, including the local poloidal flow shear.
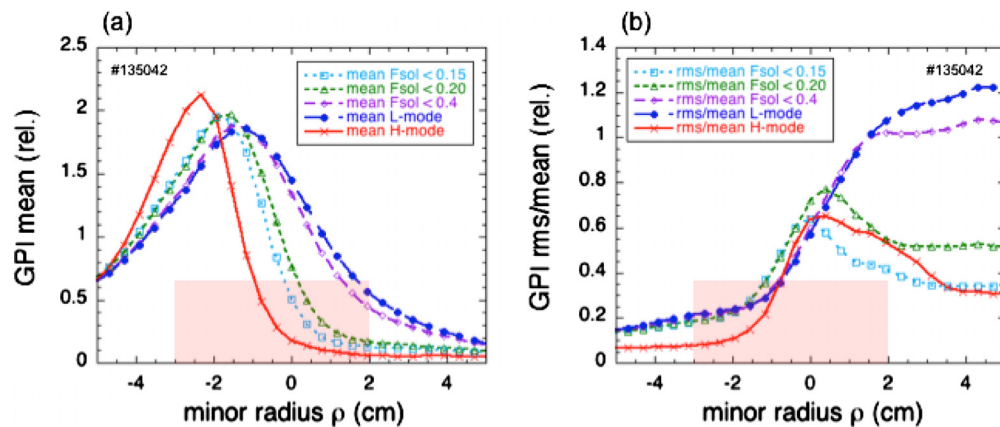
IV. TURBULENCE CORRELATIONS AND SHEAR FLOWS

Figure 10(a) shows the time dependence of the fraction of GPI light outside the separatrix F_{sol} during an ~3.5 ms period just before and across the L-H transition, along with several other turbulence properties computed from the same GPI image data for shot 135042. Figure 10(b) shows these same quantities over a longer 17.5 ms period for the same shot. All of these turbulence quantities were evaluated near the separatrix at $\rho=0.4$ cm. They were averaged over the vertical (i.e., poloidal) range shown in the analysis box in Fig. 2, and also averaged over a time interval of ~40 μs around each time point. The calculation methods for the turbulence quantities are described in the Appendix. The vertical shaded regions in Fig. 10(a) approximately mark the quiet periods near the minima of F_{sol}. The L-H transition occurs just after the last quiet period at ~0.2455 s in this shot, as shown by the vertical line.

At the top left of both Figs. 10(a) and 10(b) is the time dependence of F_{sol} (same as the top panel of Fig. 6), and just below that is the estimated poloidal turbulence velocity V_{pol} within this same region, as calculated from time-dependent cross-correlation functions in the poloidal direction (see Appendix). The poloidal velocity oscillates from $V_{pol}\sim-2$ km/s between quiet periods to $V_{pol}\sim+4$ km/s during the quiet periods, where positive V_{pol} corresponds to the electron diamagnetic direction. Note that a velocity in the electron diamagnetic direction corresponds to a potential which is increasingly negative farther into the plasma, which is the direction seen in the shear layer inside the separatrix of many previous fusion devices.[9–11]

Below V_{pol} in Figs. 10(a) and 10(b) is the autocorrelation time τ, which is also modulated at the frequency of the quiet periods, with the largest τ near or just before the beginning of the quiet periods. At the top right of Fig. 10 are the poloidal and radial correlation lengths L_{pol} and L_{rad}, again evaluated at $\rho=0.4$ cm. Both the poloidal and radial correlation lengths tend to increase just before the quiet periods; for example, the poloidal correlation lengths can increase
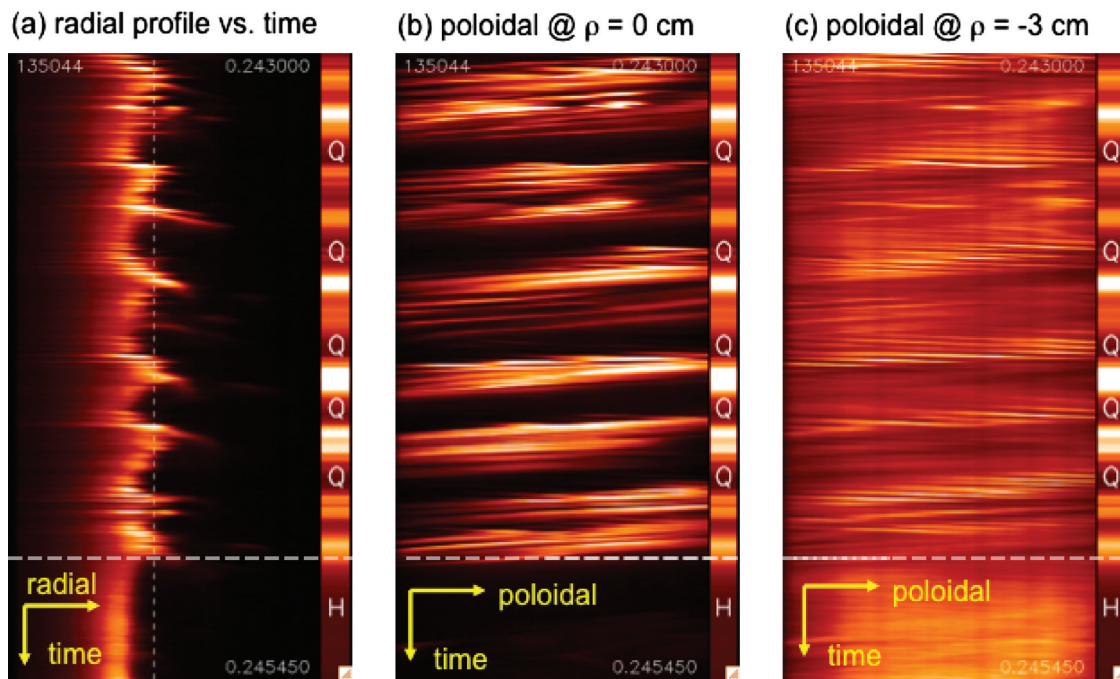

FIG. 7. (Color online) Radial profiles and relative fluctuation levels of the GPI data for #135042 during an ~10 ms period preceding the L-H transition, sorted according to F_{sol} (fraction of GPI light located outside the separatrix). Part (a) shows that the average radial profile in L-mode ("mean L-mode") is significantly broader than during H-mode ("mean H-mode"), but the quiet periods in L-mode with $F_{sol}<0.2$ look similar to the H-mode profiles. Part (b) shows that the relative GPI fluctuation levels for $F_{sol}<0.2$ are also similar to H-mode fluctuation levels, i.e., smaller than L-mode in the SOL. The shaded region shows the location of the steep density gradient region in the H-mode phase of the discharge.

FIG. 8. (Color) Fast time dependence of the radial and poloidal profiles of the GPI data between ~2 ms before to ~0.5 ms after the L-H transition for shot 135044. Part (a) shows the time dependence of the GPI light vs radius across a row of pixels at the vertical center of the images, part (b) shows same time dependence of the GPI light vs poloidal distance down a column of pixels near the separatrix at $\rho \sim 0$ cm, and part (c) shows time dependence of the GPI light vs poloidal distance down a column of pixels well inside the separatrix at $\rho \sim -3$ cm. The corresponding F_{sol} levels are shown in the bars at the right, where white is $F_{sol}=1$ and black is $F_{sol}=0$. The quiet periods are labeled with a Q, the H-mode period is labeled as H, the L-H transition is the horizontal dashed line, and the separatrix is the vertical dashed line.

from ~4 to ~10 cm. Thus all of these turbulence quantities are partially modulated with the quiet periods in F_{sol} and the reversals in the direction of V_{pol} at this radius. The cross-correlations of various turbulence quantities with F_{sol} as a function of radius are described in more detail below.

At the bottom right of Figs. 10(a) and 10(b) are the "normalized shear," defined here as $S=(dV_p/dr)(L_r/L_p)\tau$, which is a measure of the dimensionless poloidal flow shear determined from the turbulence itself (i.e., not from the plasma ExB flow speed). The quantity S measures the degree to which the average poloidal flow shear tends to distort a turbulent structure within an autocorrelation time at a fixed

point, and is closely related to the shear-flow stabilization criterion of the theoretical references.[14,16] Note that the time-scale used in evaluating S is the autocorrelation time measured at a fixed point in the GPI image, as discussed in Sec. VI D. The local radial velocity gradient in S was evaluated by a linear fit to the poloidally averaged poloidal velocities over a radial range of $\delta\rho \sim 1.5$ cm centered at $\rho=0.4$ cm. The velocity gradients found using wider radial ranges of $\delta\rho \sim 3$ cm and $\delta\rho \sim 5$ cm were well correlated with these found using $\delta\rho \sim 1.5$ cm, but systematically up to ×2 smaller, as discussed in the Appendix.

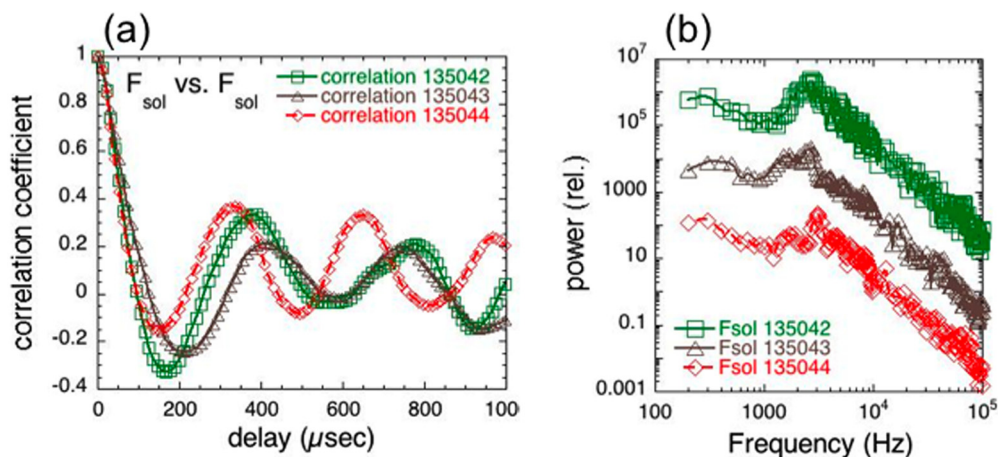Typical values for the pre-transition quantities entering S

FIG. 9. (Color online) In (a) are the autocorrelation functions of F_{sol} vs delay time for the three shots of Fig. 6, averaged over 10 ms preceding the L-H transition, and in (b) are the power vs frequency spectra of F_{sol} for the same data. The autocorrelation functions all have a quasiperiodic structure with a period corresponding to a frequency of ~3 kHz. This periodicity of the quiet times in the SOL is also visible in the raw data of Figs. 5 and 8.
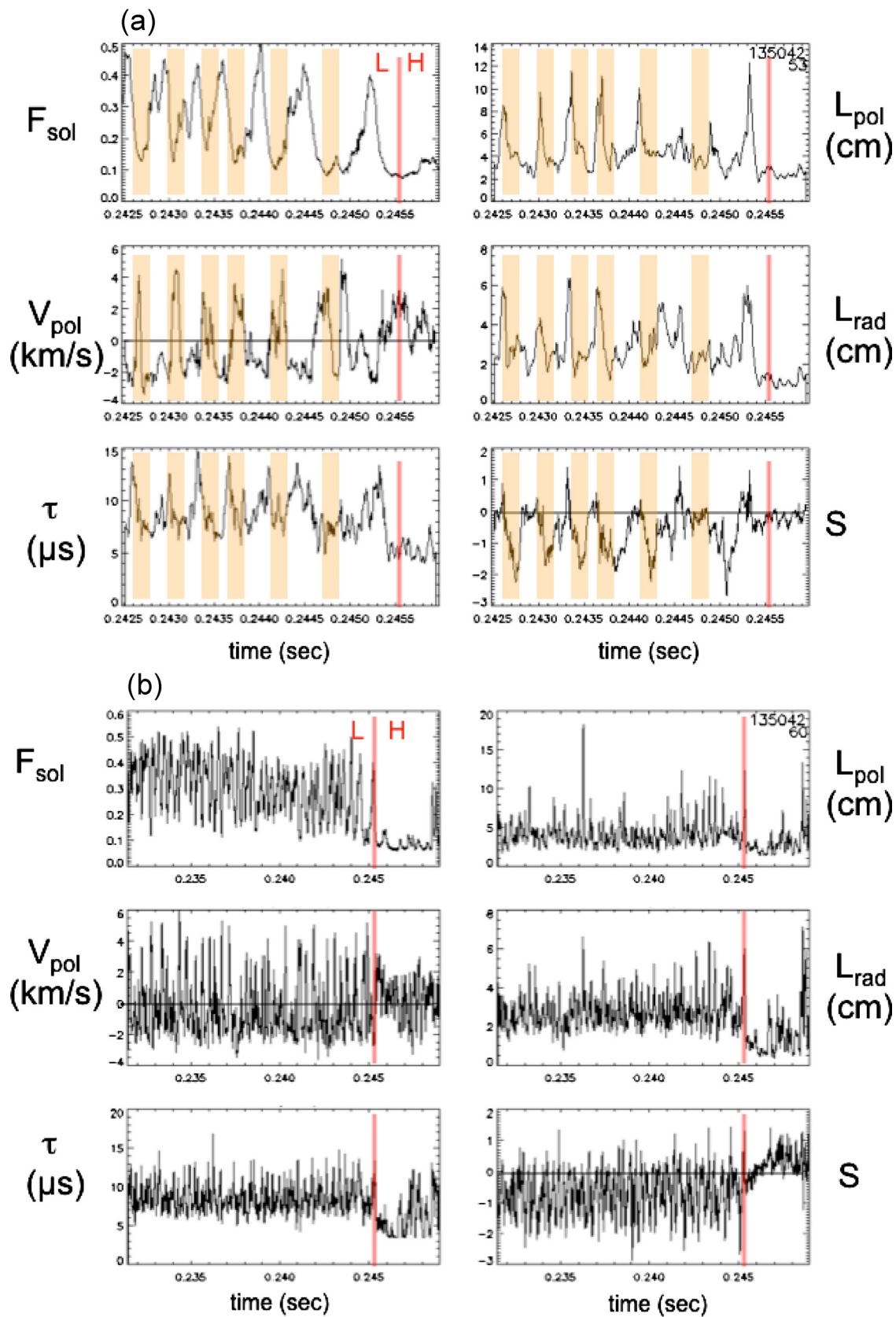
FIG. 10. (Color online) Part (a) shows the time dependence F_{sol} during an ~3.5 ms period across the L-H transition for shot 135042 for $\rho=0.4$ cm (just outside the separatrix), along with several other turbulence properties computed from the same GPI image data. The approximate time of the quiet periods is marked with shaded vertical bars in part (a), and the L-H transition with a thin vertical bar. Part (b) shows these same quantities over a longer 17.5 ms period for the same shot. These turbulence quantities averaged over a time interval of ~40 μs around each time point. Positive V_{pol} corresponds to the electron diamagnetic direction.
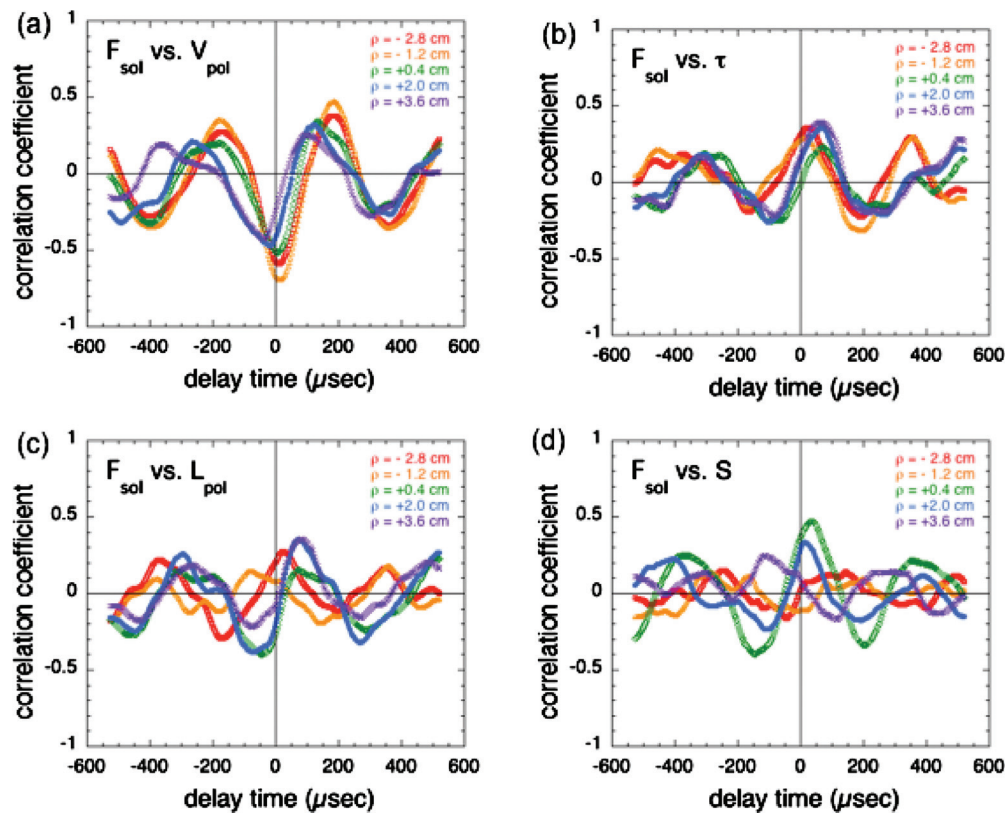
FIG. 11. (Color) Time-delayed cross-correlation functions between F_{sol} and other turbulence quantities during a 3.5 ms period just preceding the L-H transition in #135042 (0.239 505–0.243 005 s): (a) F_{sol} vs V_{pol}, (b) F_{sol} vs τ, (c) F_{sol} vs L_{pol}, and (d) F_{sol} vs S. For this figure the cross-correlations are shown for five adjacent radial regions within the box in Fig. 2, including the case for $\rho = 0.4$ cm used for Fig. 10 (green). The cross-correlations of F_{sol} and V_{pol} all show a peak near zero delay, but the time of this peak correlation changes systematically with radius. Cross-correlations of F_{sol} and S are strongest near the separatrix.

in the data of Fig. 10 are $L_p \sim 4$ cm, $L_r \sim 3$ cm, $\tau \sim 8$ μs, and $dV_p / dr \sim -1 \times 10^5$ s^{-1}, leading to a typical value of $S \sim -1$. The range of S for the L-mode phase is mainly between $S \sim -2$ and 1. Inspection of Fig. 10(a) indicates that S reverses sign near the time of the quiet periods, similar to the poloidal velocity. From Fig. 10(b) it can be seen that the average behavior of S does not vary significantly over ~ 15 ms preceding the L-H transition, again with no sign of a trigger mechanism for the transition. Although the poloidal velocity and S appear to change sign after the L-H transition, the turbulence analyses for τ, L_r, and S are not reliable during H-mode since the turbulence is too small to analyze at this radius; thus the changes from L-mode to H-mode in this case should be considered only qualitative.

Figure 11 shows the time-delayed cross-correlation functions between F_{sol} and several other turbulence quantities during the 3.5 ms period just before the L-H transition in #135042 (0.239 505–0.243 005 s). In this figure the cross-correlations are shown for five different radial locations within the box in Fig. 2, including the region at $\rho = +0.4$ cm used for Fig. 10 (in green). The cross-correlations of F_{sol} and V_{pol} in (a) all show a negative peak near zero time delay, indicating at least a 50% correlation between the quietest periods (minimum F_{sol}) and the most positive V_{pol} (i.e., electron diamagnetic flow), which also can be seen in the raw data in Fig. 8. It is interesting that the peak correlation coefficient changes systematically with radius, with the largest correlation occurring at radii well in-

side the separatrix ($\rho = -1.2$ to -2.8 cm). At these radii the maximum cross-correlation between F_{sol} versus V_{pol} occurs at a *positive* time delay, which implies that the positive peak of V_{pol} lags behind the negative peak of F_{sol}. However, at radii in the SOL, e.g., $\rho \sim +2.0$ and +3.6 cm, the maximum correlation occurs at a *negative* time delay, implying that positive peak in V_{pol} leads the minima of F_{sol}. Thus a unique causal relationship between V_{pol} and F_{sol} can not be determined from these cross-correlation maxima, since the sign of their relative time delay changes with radius.

The maximum cross-correlation coefficients between F_{sol} and τ, and between F_{sol} and L_{pol}, are weaker than those between F_{sol} and V_{pol}, but also have a complex variation with radius, as shown in Figs. 11(b) and 11(c). For comparison of these results with the shear-flow stabilization model the cross-correlations of F_{sol} and S are of the most interest, as shown in Fig. 11(d). This correlation is strongest near or just outside the separatrix; for example, at $\rho = +0.4$ cm this is about 0.5, when S lags F_{sol} by 14 μs, and there is little or no significant correlation between F_{sol} and S inside the separatrix for this shot. Thus at the location where the correlation between F_{sol} and V_{pol} is large ($\rho = -1.2$ to -2.8 cm), the correlation between F_{sol} and S is small.

Figure 12 shows the time evolution of several of the quantities of Fig. 11 with respect to the L-H transition time for the three shots of Fig. 9 for $\rho \sim +0.4$ cm. Each point in Fig. 12 averages over 3.5 ms (1000 frames), which includes ~ 10 cycles of the ~ 3 kHz oscillation. Figure 12(a) shows
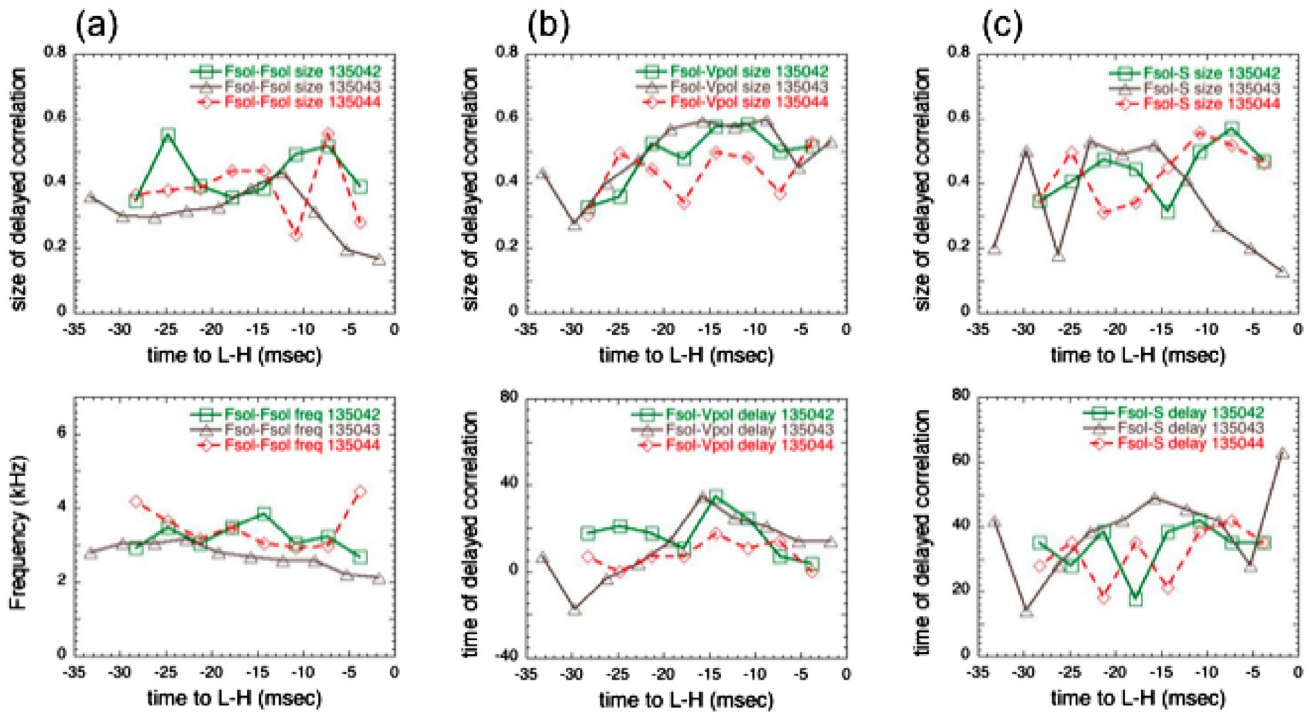
FIG. 12. (Color online) The time evolution of several of the quantities of Fig. 11 for the radius $\rho=0.4$ cm during the ~30 ms preceding the L-H transition for the same three shots as in Fig. 9. In part (a) is the magnitude of the first negative peak of the autocorrelation function of F_{sol}, which is a rough measure of the size of the oscillating feature at ~3 kHz, and below that is the corresponding frequency of this feature. In part (b) is the magnitude of the peak of the cross-correlation functions between F_{sol} and V_{pol} near zero delay time, and below that is the delay time to this peak. In part (c) is the magnitude of the peak of the cross-correlation functions between F_{sol} and S (near zero delay), and below that the delay time to this peak.

the magnitude of the first negative peak of the autocorrelation function of F_{sol} [e.g., at 165 μs for #135042 in Fig. 9(a)], which is a rough measure of the size of the quasiperiodic feature at ~3 kHz; below that is the corresponding frequency of this feature. Neither of these quantities change systematically over ~30 ms preceding the L-H transition. In Fig. 12(b) is the magnitude of the peak of the cross-correlation functions between F_{sol} and V_{pol} (nearest zero delay time), and below that is the delay time to this peak. The size of the correlation between F_{sol} and V_{pol} does not change systematically during the 20 ms before the transition, but does seem to increase during the 30–20 ms before the transition. Finally, in Fig. 12(c) is the magnitude of the peak of the cross-correlation functions between F_{sol} and S (nearest zero delay time), and below that the delay time to this peak. Neither of these quantities change systematically over ~30 ms preceding the L-H transition. Thus there is no clear and consistent change in these correlations over during the 20 ms preceding these L-H transitions. Since the transitions happen so rapidly (≤1 ms), this strongly suggests that the quiet periods do not cause or trigger the transition (as discussed in Sec. VI A).

Finally, Fig. 13 shows scatter plots of the correlation between F_{sol} and V_{pol} (top) and F_{sol} and S (middle) for the same $\rho=0.4$ cm case used for Fig. 11. Here both plots show all 1000 time points within a 3.5 ms period ending ~2 ms before the transition, with a small correction to align the time at the peak of their cross-correlations of Fig. 11. There is clearly only a partial correlation between V_{pol} and F_{sol} in this

(and all other) data, but with a trend for low values of F_{sol} to occur at positive V_{pol}, as can also be seen in Fig. 10(a). There is a rather wide scatter of F_{sol} versus S (right), independent of the radial averaging width $\delta\rho$ used for dV_{pol}/dr (middle versus bottom). Thus there is only a partial correlation between S and F_{sol} in these data.

In summary, the ~3 kHz quiet periods preceding the L-H transition as measured by the parameter F_{sol} are at least partially correlated with local changes in the turbulence parameters such as V_{pol}, τ, and L_{pol}, as illustrated in Fig. 10. The cross-correlations between these parameters and F_{sol} varied systematically with radius near the separatrix, as shown in Fig. 11, and there was no single consistent causal (i.e., temporal) relationship between the peaks in F_{sol} and those in V_{pol} or S. For the three shots examined in detail in Fig. 12, there was little or no systematic variation of the correlations between F_{sol} and V_{pol} or S during the ~20 ms period preceding the main L-H transition, and Fig. 13 showed that there was only a modest correlation between the magnitudes of F_{sol} and those of V_{pol} and S during a 3.5 ms preceding the transition. Thus there is good evidence for a correlation between the quiet periods and the local edge turbulence, but no clear evidence for a trigger mechanism for the main L-H transition in these data. A larger data set is examined in Sec. V, and a more detailed study of the space/time correlations between the quiet periods and the turbulence will be described in a future paper based on a 2-D velocimetry analysis.[43]
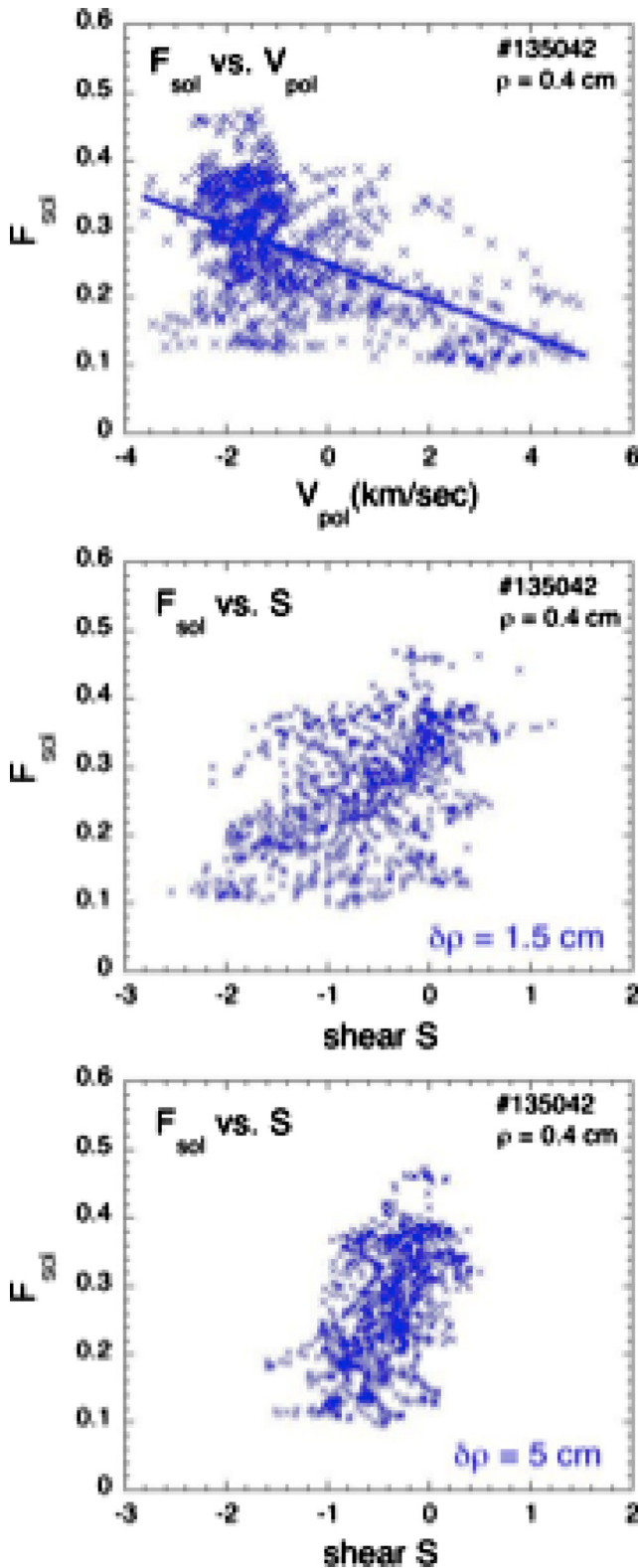
FIG. 13. (Color online) Typical scatter plots of the correlation between F_{sol} and V_{pol} (top), F_{sol} and S with $\delta\rho = 1.5$ cm (middle), and F_{sol} and S with $\delta\rho = 5$ cm (bottom). All cases are for $\rho = 0.4$ cm (as in Fig. 11), and all have 1000 time points within a 3.5 ms period ending ~ 2 ms before the transition. All points are at the time of the peak of the cross-correlation functions. There appears to be a significant statistical correlation between quiet periods with low values of F_{sol} and a positive V_{pol}, as can also be seen in Fig. 10(a), as shown by the linear fit to these data. There is a rather wide scatter of F_{sol} vs S for both values of the radial averaging width $\delta\rho$ used for dV_p/dr (middle and bottom).

V. LARGER DATABASE

Table I lists the 16 shots in this database, i.e., nine shots with L-H transition captured at the highest available frame rate of (3.5 μs/frame), four shots with L-H transitions captured at a slower frame rate, two shots in L-mode only, and one shot in H-mode only. These data were analyzed in the same way as #135042–135044 for Figs. 10–12 to check whether the trends described in Sec. IV were typical.

Figure 14 shows the analysis of the size and frequency of the ~ 3 kHz quiet feature with respect to the L-H transition time for all of these shots, including the data previously shown in Fig. 12(a). At the left is the magnitude of the first negative peak of the autocorrelation function of F_{sol}, which is a rough measure of the size of the quasiperiodic feature at ~ 3 kHz, and at the right is the frequency of this feature as determined from the delay time of this peak. The two L-mode shots are arbitrarily set at -150 ms and the one H-mode shot is arbitrarily set at $+50$ ms in order to put them on the same plot as the other data. There appears to be no systematic change in the size or frequency of the ~ 3 kHz feature during the ~ 40 ms preceding the L-H transition, consistent with Fig. 12. However, there is a significant scatter in the size and frequency over this time period, which may be due to a modulation in the amplitude of the quiet feature, analogous to that seen for the GAM.[6,26,29] Also, a qualitatively similar ~ 3 kHz feature appears in the few L-mode and H-mode shots examined, implying that the quiet periods occur independently of the L-H transition. Note that the relatively few data points in Fig. 14 between -50 and -150 ms before the transition are due to lack of GPI data at these times, and not the absence of an ~ 3 kHz feature in the GPI data.

Figure 15 shows the time dependences of F_{sol} and S before the L-H transition for two other high speed shots besides #135042 [already shown in Fig. 10(b)]. Although there is a strong modulation of S with F_{sol} at ~ 3 kHz, as in Fig. 10, there appears to be no systematic change in S within ~ 15 ms of the transition for these cases, or for any of the nine shots with the fastest framing rate, consistent with Fig. 10. Note that the two shots in Fig. 15 do not show any systematic decrease in F_{sol} during the few milliseconds before the transition, as seems to be the case for the three shots in Fig. 6.

Figure 16 shows the estimated S versus time for three different radial locations for the time period from 1.5 ms before the transition to 0.5 ms after the transition, namely, $\rho = -2.8$ cm (well inside the separatrix), $\rho = 0.4$ cm (near the separatrix), and $\rho = +3.6$ cm (well outside the separatrix). For each of these radii the result for shot 135042 is at the left, and a superposition of all nine shots with the fastest framing rate is at the right. Although there are some transient increases in the negative shear for a few of these shots at $\rho = 0.4$ cm during the 1.5 ms preceding the transition, there appears to be no consistent and reproducible change in S before the transition which could be identified as a trigger mechanism for these L-H transitions. This conclusion is unchanged by the ± 0.2 ms uncertainty in the identification of the exact time of the L-H transition, as discussed in Sec. III.
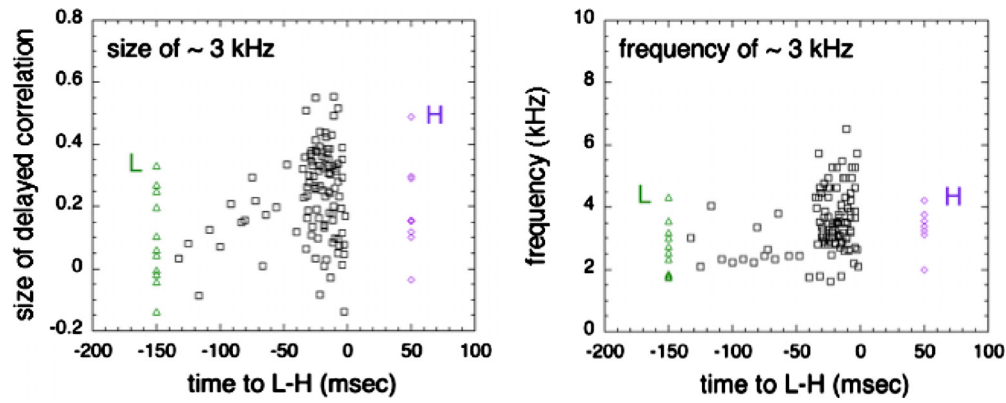
FIG. 14. (Color online) Analysis of the size and frequency of the ~3 kHz quiet feature vs time for a larger database of shots, including the data previously shown in Fig. 12(a). The L-mode shots are put at −150 ms and the H-mode shot is put at +50 ms to bring them into the same plot. There is no clear change in the size or frequency of the ~3 kHz feature during the ~40 ms preceding the L-H transition, consistent with the trend seen in Figs. 10 and 12. The ~3 kHz feature also appears in L-mode and H-mode shots, so it does not appear to be a feature specific to the L-H transition.

VI. DISCUSSION

A. Summary of results

This paper described the first NSTX observations of quiet periods of reduced edge turbulence preceding the L-H transition, as diagnosed by the GPI diagnostic near the outer midplane separatrix. These quiet periods were quantified by a parameter F_{sol}, which measured the fraction of the GPI D_α light emission occurring outside the separatrix. During quiet periods the GPI light emission pattern was transiently similar to that seen during H-mode, i.e., with a small fraction of the GPI light emission located outside the separatrix, as shown in Figs. 4–7. These quiet periods had a frequency of ~3 kHz and were observed for at least 30 ms before the L-H transitions, as shown in Figs. 8–12. There was evidence that similar quasiperiodic oscillations occurred during L-mode shots without any L-H transition, as shown in Fig. 14. Thus these quiet periods appear to occur independently of the L-H transition, and so do not seem to be an obvious trigger or cause of the L-H transition in NSTX.

The quiet periods were least partially correlated with local changes in the turbulence parameters such as the poloidally averaged V_{pol}, τ, and L_{pol}, as shown in Figs. 10–13. The cross-correlation coefficient and phase between F_{sol} and V_{pol} changed systematically with radius over the range of radii $\rho=-2.8$ to 3.6 cm, as shown in Fig. 11(a), which indicates a variation across the separatrix of the phase of the poloidal flow associated with the quiet periods. There were also lower cross-correlations between F_{sol} and the other turbulence quantities such as L_{pol} and τ, as shown in Figs. 11(b) and 11(c). Thus the quiet periods were associated with a complex set of changes in the turbulence structure and motions, which will be examined in detail elsewhere using a higher resolution velocimetry code.[43]

The paper also analyzed the turbulence in the GPI images to obtain an estimate for the dimensionless poloidal shearing $S=(dV_p/dr)(L_r/L_p)\tau$, which is an approximate measure of the extent to which the average poloidal flow shear distorts a turbulence structure within a local turbulence autocorrelation time. The strongest time variation in S was correlated with the quiet periods, during which time the po-
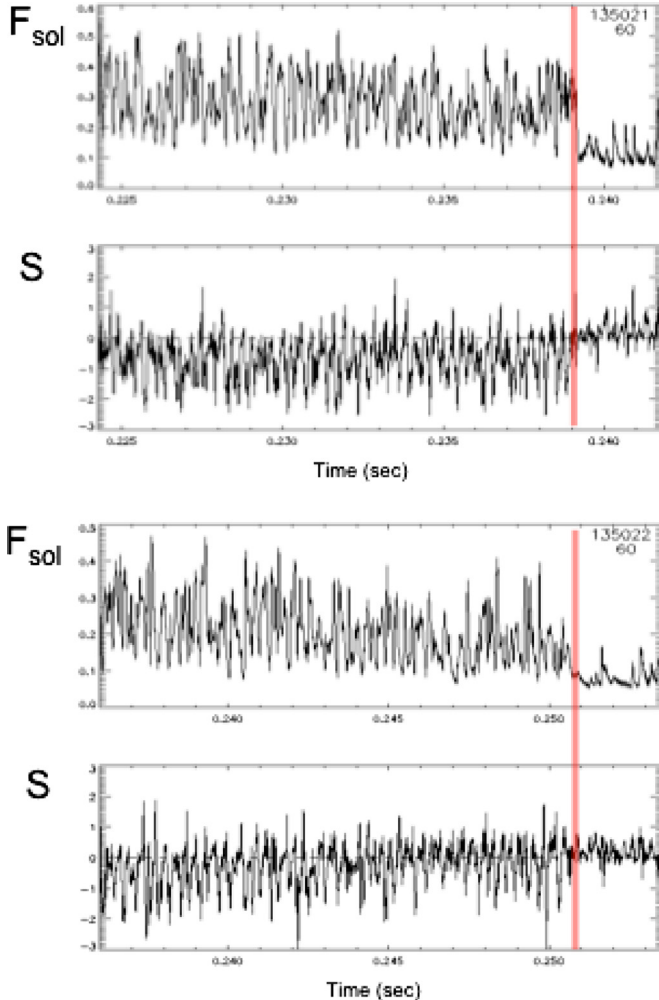

FIG. 15. (Color online) Time dependences of the SOL fraction F_{sol} and the normalized shear S for a period of ~15 ms before the L-H transition (vertical lines) for two additional shots besides #135042 [already shown in Fig. 10(b)]. Although there is a strong modulation of S with F_{sol} at ~3 kHz for at least 15 ms before the transition, there are no clear variations in the average value of F_{sol} or S on this timescale, consistent with Figs. 10 and 12. A radial averaging of $\delta\rho \sim 1.5$ cm was used for the velocity gradient in this analysis.
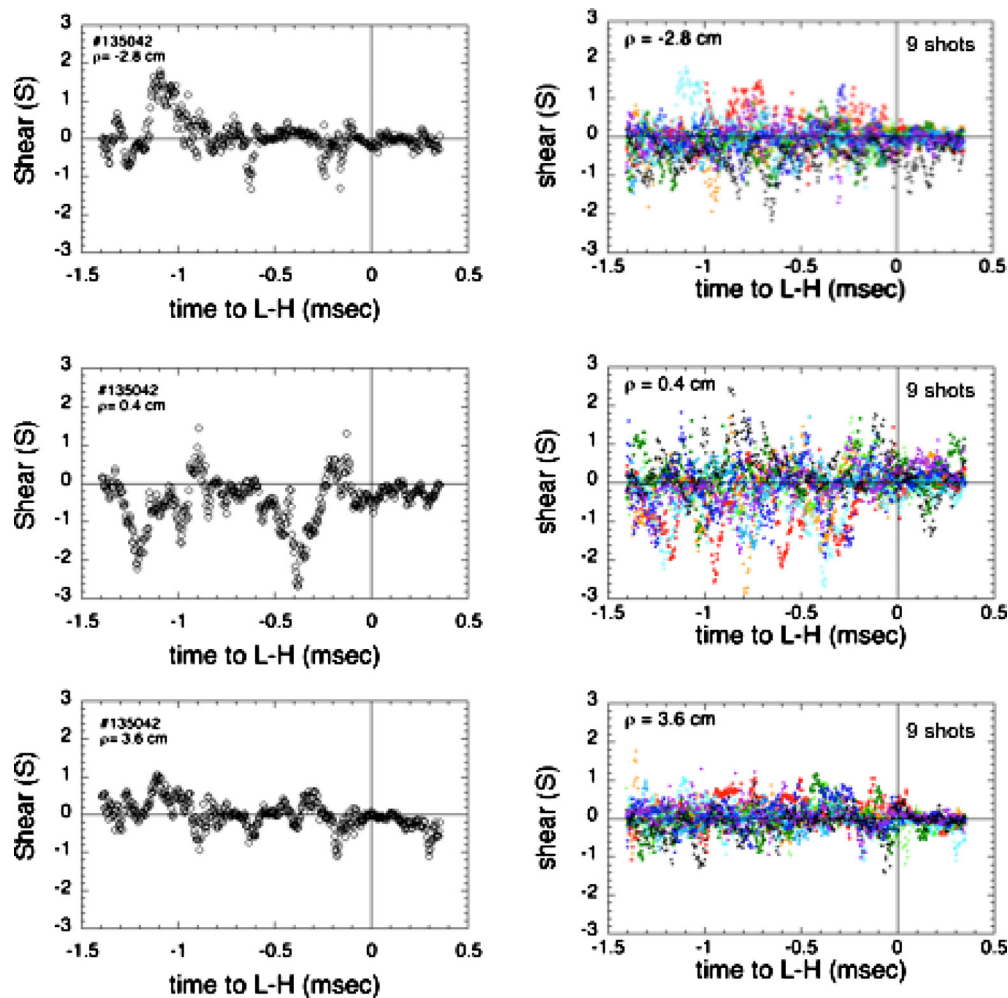
FIG. 16. (Color online) The normalized shear S for the time period up to ≤1.5 ms before the transition for three radial locations for #135042 (left) and for the superposition of all nine shots at the highest frame rate at the same radii (right). There is again no clear variation in S before the transition which could be considered as a trigger for the L-H transition. A radial averaging of $\delta\rho \sim 1.5$ cm was used for the velocity gradient in this analysis.

loidal velocity and S reversed sign, corresponding to a flow in the electron diamagnetic direction near the separatrix during the quiet times. Apart from this ~3 kHz modulation, there was no systematic time variation of S within a ~20–30 ms preceding the L-H transition, at least within the region of ±3 cm around the separatrix, as shown in Figs. 14–16.

    Thus these measurements provide the first evidence for a "zonal flow" located near the separatrix of NSTX, in which reversals in the direction of poloidal flow are correlated with changes in the local turbulence. This behavior is qualitatively consistent with the general "drift-wave-zonal-flow paradigm" described in several recent review papers.[9,10,22,23]

    On the other hand, these measurements do not provide a clear identification of a trigger mechanism or local cause for the main L-H transition in NSTX. There was little or no systematic variation of the quiet periods or the dimensionless poloidal flow shear during the ~20–30 ms immediately preceding the transition. This suggests that the L-H transition is either caused by a very slow and/or very small variation in the local turbulence, or by some phenomenon outside the range of the GPI diagnostic view. An assessment of the rela-

tionship between the present results and previous experiments and theory in this area is presented in Secs. VI B and VI C, respectively, and a discussion of the uncertainties and limitations of these measurements and analysis is in Sec. VI D.

B. Relation to previous experimental results

    There have been many previous measurements of low frequency zonal flows and their correlations with higher frequency turbulence in tokamaks and other plasma devices, as discussed in Sec. I and extensively reviewed in Refs. 9, 10, 22, and 23. The results described in Secs. III–V show that these NSTX quiet periods and poloidal flows behave similarly to the zonal-flow-drift-wave interaction discussed in the references cited above. In NSTX the quiet periods correspond to a reduced level of SOL turbulence and its associated radial transport in the SOL, and the local poloidal flow corresponds to the global zonal flows found in the previous experiments.[24–33]

    However, in NSTX the global nature of the zonal flows seen in previous experiments has not yet been clearly iden-

tified since the GPI diagnostic has only a limited range in poloidal angle over which the flow was observed. Also, the frequency spectra of the quiet periods/poloidal flows observed in NSTX (e.g., Fig. 14) are broader than those seen for GAMs in other tokamaks,[24–32] so it is not yet clear whether the oscillations in NSTX are GAMs broadened by the low aspect ratio of NSTX, or the broadband lower frequency, zonal flows such as seen, for example, using BES in DIII-D,[30] reflectometry in ASDEX Upgrade,[31] and probes on HL-2A.[33] This is discussed further in Sec. VI C.

The literature on edge turbulence in tokamaks also includes analyses of quiet-time statistics between successive bursts of turbulent flux in JET and other devices.[44] However, that analysis found a continuous distribution of quiet times and not a quasiperiodic oscillation in quiet times, as found here (e.g., Fig. 9). Also, that analysis was focused on comparisons with self-organized criticality or rescale adjusted range (R/S) models, and not with poloidal flows or local shear, as described here.

There have been many previous experimental results concerning changes in edge turbulence associated with the L-H transition, as reviewed extensively in Refs. 2 and 8–10. The sudden reduction in the level of edge turbulence at the transition seen previously (e.g., Refs. 4–7) is also seen in the present NSTX results (e.g., Fig. 8). Changes in the poloidal shear flow before versus after the transition were also observed previously,[34–37] but a fast time-resolved analysis of the local dimensionless shear preceding the transition including the radial correlation length (e.g., Figs. 15 and 16) has not been done previously. The absence of a systematic change in this shear parameter preceding the L-H transition appears to provide a counterexample to the usual model of shear-flow stabilization as the cause of the L-H transition. However, note that the turbulence shear estimates here were not reliable after the L-H transition (see Sec. IV), and that no direct measurements were made of the plasma flow speed or the radial electric field, which in other experiments were used to evaluate the shear flow and shear layer development during the transition (e.g., Refs. 4, 5, 7, and 10).

A strong correlation between externally imposed changes in the radial electric field caused by electrode biasing and H-mode-like transitions has been seen in several previous experiments.[45] However, the relationship between the electrode biasing transition and the spontaneous L-H transitions seen here in NSTX is not quite clear, since no similar biasing experiments have been done on NSTX.

Previous GPI measurements of turbulence on NSTX (Ref. 38) used high speed cameras with only 300 frames at 250 000 frames/s (1.2 ms), so did not identify the slowly oscillating quiet periods described here. However, the poloidal array of PM tubes did detect some transient reversals in V_{pol} preceding the L-H transition (Fig. 6 of Ref. 38), which are similar to those shown in more detail in Fig. 10 here. A previous evaluation of the turbulence bicoherence done using GPI in NSTX showed no systematic changes preceding the L-H transition,[39] consistent with the absence of systematic changes in the shear flow presented here.

C. Relationships to theory and simulation

The principal theoretical question about these results concerns the physics of the ~3 kHz quiet periods and poloidal flow reversals seen in the GPI data preceding the L-H transition. Given the recent large body of experimental and theoretical work in the area of zonal flows, as reviewed in Refs. 22 and 23, it is plausible that this is a zonal flow or a GAM.

A preliminary calculation of the GAM frequency for NSTX was done by solving the eigenvalue problem given by the two-fluid equations as used in the NLET code[46] for zero radial wave number, with the result

$$f(\text{Hz}) = Gc_s/(\pi R), \tag{1}$$

where R is the major radius at the outboard midplane of the considered flux surface, c_s is the thermal speed $[\gamma(T_i + T_e)/m_i]^{1/2}$, γ is the adiabatic exponent of the system (ranging between 1 and 5/3 for isothermal and adiabatic systems, respectively), and G is the geometry dependent factor determining the GAM frequency.

The GAM originates from the coupling between sound waves and poloidal rotation induced by the toroidal curvature. While in a large aspect ratio tokamak with circular flux surfaces, the poloidal rotation couples in principle only to the sinusoidal ($n=0$, $m=1$) pressure perturbation resulting in one high frequency mode—the GAM—in more complicated setups as in NSTX, the poloidal rotation can couple to several sound modes resulting in several modes which to some extent show GAM behavior. The "GAM-ness" of those modes can be classified by the ratio of the energy of the poloidal flow to the parallel kinetic energy of the mode, E_{perp}/E_{par}. Modes with $E_{perp} > \sim E_{par}$ can be called GAMs whereas modes with $E_{perp} \ll E_{par}$ are practically sound waves.

The frequency spectrum for NSTX near the separatrix calculated this way contains three modes that can be considered GAMs, namely, $G \sim 0.49$, 0.31, and 0.65 with $E_{perp}/E_{par} \sim 1.48$, 1.03, and 0.67, respectively. Due to the similar ratios E_{perp}/E_{par} in principle all three modes can be present in a turbulent system. Eventually, the properties of the turbulence decide whether one mode is excited preferentially. The T_e measured by Thomson scattering at the separatrix in L-mode was ~50 eV (Fig. 3). Thus, assuming $T_i \sim T_e$ and $R=1.5$ m, the expected GAM frequency is in the range of ~4.6–12.3 kHz for the three GAM candidates (using $G=0.31$ with $\gamma=1$ and $G=0.65$ with $\gamma=5/3$). Numerical three-dimensional (3-D)-turbulence studies using NSTX geometry performed with NLET show that the "low frequency" GAM candidate is excited by the turbulent modes. The observed GAM frequency of $f \sim 6.3$ kHz at $T_e=50$ eV is slightly higher than the upper limit of the mode with $G \sim 0.31$ predicted from the linear calculation above. Hence, the GAM frequency predicted by NLET is of the same order as the frequency of the quiet periods, which is quite good agreement, considering the large temperature variation of $T_e \sim 10$–100 eV within ± 2 cm around the separatrix.

In a separate calculation of edge turbulence in NSTX made using the 2-D electrostatic edge "scrape-off layer turbulence" code SOLT,[47] low frequency zonal flows correlated

with modulations of the turbulence level were observed in some cases at a frequency of ~ 4 kHz, which is very similar to the frequency of the quiet periods and poloidal flows described in the present paper. The relationship between these SOLT results and the present GPI results will be described in a subsequent publication.

D. Uncertainties and limitations

The main uncertainty in the present measurements concerns the absence of a direct measurement of the changes in edge plasma parameters during the quiet periods. Although the measured D_α light is a well known function of the atomic physics $f(n_e, T_e)$,[42] there is no way at present to determine whether GPI profile changes during quiet periods are due to density or temperature changes (or both). Thus the evaluation of fluctuating plasma-dependent quantities such as the collisionality or β can not be done. However, turbulence properties such as the correlation lengths, times, velocities, and hence the normalized shear are independent of the nonlinearities in the $f(n_e, T_e)$ (Ref. 40) and can be evaluated directly from the GPI data.

The location of the separatrix, which has been evaluated here using the NSTX equilibrium model (i.e., magnetic measurements supplemented by Thomson scattering profiles), is uncertain by roughly ± 1–2 cm. However, even though the numerical value of the "H-mode-ness" parameter F_{sol} used here (e.g., in Fig. 6) depends on the separatrix location, the relative time dependence and spectrum of F_{sol} do not, at least within this range of uncertainty; therefore all of the results derived from F_{sol} are to a good approximation independent of the separatrix uncertainty.

The estimate the local poloidal flow shear $S = (dV_p/dr) \times (L_r/L_p)\tau$ used in this paper, which was motivated by theories of the H-mode transition such as the Biglari–Diamond–Terry model,[16] is clearly uncertain in several ways. The autocorrelation time at a fixed point in space τ used here can be affected by both the intrinsic lifetime of the structure τ_{life} and also by the time for the structure to propagate past a fixed point τ_v. Following the analysis of Ref. 48, these times can be related as $\tau = \tau_{life} \; \tau_v / (\tau_{life}^2 + \tau_v^2)^{1/2}$. In the NSTX case, $\tau_v \sim L_{pol}/V_{pol} \geq (4 \text{ cm})/(2-4 \times 10^5 \text{ cm/s}) \sim 10$–20 μs, which is somewhat larger than the measured τ. Thus, if the theory requires the use of τ_{life} rather than τ, the S values here are slightly underestimated (as they have been in all previous estimates of local turbulence shearing).

Typical statistical uncertainties in the estimation of GPI correlation lengths and times and poloidal velocity can be seen in Fig. 10(a) in between the quiet periods, and are roughly $\pm 10\%$–20% for the chosen averaging interval of ~ 40 μs. The estimation of the gradient in poloidal velocity requires an additional averaging over some radial range, which was normally chosen to be the smallest plausible value of ~ 1.5 cm (4 pixels). The variation in S was reduced by about a factor of 2 when this radial averaging range was increased to ~ 5 cm, as shown in Fig. 13. Thus the estimate of S is uncertain by at least a factor of 2 due to the uncertainties in L_{pol}, L_{rad}, τ, and dV_{pol}/dr. This uncertainty contributes to the wide scatter in the F_{sol} versus S plots in Fig.

13, and the less-than-perfect correlations of Fig. 11. However, the plots of Fig. 11 clearly show statistically significant time-averaged cross-correlations between the various turbulence quantities, as described in Sec. IV.

Additional limitations of the present results come from the relatively small fraction of the edge which is diagnosed by GPI in NSTX (Fig. 1). Although the poloidal flow measurements are averaged over an ~ 20 cm poloidal range within the GPI view (Fig. 2), and so represent an average flow over a region which covers ~ 4–5 poloidal correlation lengths of the turbulence, the global nature of the zonal flows has not yet been verified directly using widely separated flow measurements. Although the radial range of the GPI view covers the whole region of the H-mode pedestal (Fig. 3), the GPI signal itself was analyzed only within ± 4 cm of the nominal separatrix location (Fig. 7). Thus the full profile of the edge turbulence from the wall to the core could not be measured in this experiment.

Finally, there is presently no other diagnostic on NSTX which has been able to measure the quiet periods/poloidal flow reversals discussed in this paper. Neither the standard D_α signals (as in Fig. 3) nor the spectroscopic edge poloidal rotation diagnostics have a fast enough response to observe either the edge turbulence or the quiet periods, and no correlation of the quiet periods has yet been observed with magnetic fluctuations at the wall, with edge soft x-ray emission, or with oscillations in the separatrix location.

E. Conclusions and future work

The most interesting result from this paper was the discovery of transient quiet periods in the edge turbulence in NSTX which correlated with local reversals in the direction of the poloidal turbulence flow and flow shear, as described in Secs. III and IV. Although new to NSTX, this result is generally consistent with recent experiments and theory concerning the zonal-flow-drift-wave interaction, as discussed in the reviews.[9,10,22,23] An evaluation of the GAM frequency for NSTX was roughly consistent with the observed quiet period frequency of ~ 3 kHz, but also with a calculation of the zonal flow frequency in NSTX, as discussed in Sec. VI C.

The other main result of this paper was that the estimated shear-flow parameter S did not appear to have consistent variation preceding the L-H transition which could be identified as a trigger for the transition, as described in Sec. V. This result contrasts with the usual theoretical model in which the transition is caused by changes in the local shear flow.[2,3,7–10] However, the present result is consistent with the conclusions of two recent reviews, i.e., that the role of turbulence in triggering the L-H transition must be considered an open issue.[2,10]

Thus the first general area for future experimental work is to examine in detail the frequency spectrum and radial structure of the turbulence flows in these GPI data using a sophisticated hybrid optical flow/pattern (HOP-V) matching code,[43] which has a higher space-time resolution than the cross-correlation analysis used in the present paper. An initial comparison of the poloidal velocities inferred from that code with the present cross-correlation velocity analysis shows

good agreement, as described in the Appendix. Results from this analysis should be compared with theoretical models for GAMs and zonal flows such as those discussed in Sec. VI C. This analysis can also be used to calculate the Reynolds stress as a function of time preceding the L-H transition, as done in Ref. 35.

The second general area for future work involves continued search for a trigger mechanism for the L-H transition. One possibility is that the L-H transition does not actually have a clear trigger, but rather is caused by very slow or slight changes which cross some threshold to produce a sudden "phase transition." Another possibility is that the trigger is nonlocal, i.e., the changes seen in the GPI diagnostic were caused by events outside the field of view, e.g., far inside the separatrix or in the divertor region. A third possibility is that the trigger involves subtle changes in the edge turbulence which have not been identified by the analysis done so far. This last possibility should be considered seriously given the various uncertainties and limitations of the GPI diagnostic and analysis techniques, as described in Sec. VI D.

There are many other specific areas for future work in this area. The poloidal rotation of the turbulence seen with GPI should also be compared with spectroscopic rotation measurements and probe measurements of the radial potential profile, so that the GPI results can be compared with the evolution of the internal shear layer and with neoclassical predictions. The lifetime of the turbulent structures within the moving flow could be used to evaluate the local flow shear, rather than the local autocorrelation time. Measurements of edge turbulence at another poloidal angle could confirm the zonal nature of the quiet periods and zonal flows, and comparisons of the timing and spatial location of the quiet periods should be made between various diagnostics. Bicoherence analysis of the GPI turbulence in NSTX done previously[39] should be extended to wave number space to assess this interplay between large and intermediate scales, and the turbulent Reynolds stress should be evaluated and compared with the local poloidal flow. The scaling of the frequency and amplitude of the quiet periods should be evaluated with respect to NBI power, magnetic field q(a), beta, collisionality, and other global plasma parameters. It would also be interesting to examine the possible relationship of these quiet periods with the much slower "dithering" process often seen in L-H transitions.[2]

APPENDIX: CALCULATION OF TURBULENCE QUANTITIES

The turbulence quantities analyzed in this experiment were calculated directly from the GPI light intensity images versus time (e.g., Fig. 5). The autocorrelation times τ were calculated for each pixel as the time for the autocorrelation function to first go down to 0.5; this τ measures the short turbulence autocorrelation time of ~ 10 μs, and does not measure the much longer ~ 3 kHz oscillation. These results were then the averaged over the ~ 20 cm high poloidal range of the box shown in Fig. 2, and over ~ 40 μs in time (11 frames) to get the τ in Fig. 10. The correlation lengths were calculated as $L = 1.66(\delta x)/\mathrm{sqrt}(-\ln C_{12})$, where δx is the radial or poloidal separation between two nearby points and C_{12} is the zero-time cross-correlation coefficient between them (this assumes a Gaussian correlation function). The distances used were $\delta x \sim 1.6$ cm in the poloidal direction (4 pixels) and $\delta x \sim 0.8$ cm in the radial direction (2 pixels), i.e., both were well within a correlation length. These local correlation lengths were then averaged over the ~ 20 cm high poloidal range of the box shown in Fig. 2, and over ~ 40 μs in time (11 frames) to get the L_{rad} and L_{pol} of Fig. 10.

The poloidal velocity V_{pol} was calculated for each pixel for each frame by first calculating the one-frame-delayed cross-correlation coefficient between that pixel and nearby pixels (± 5 pixels each direction), averaging over ± 11 frames in time (± 38.5 μs). The poloidal speed for that pixel and frame is then calculated as the poloidal displacement of the peak correlation location divided by the time between frames (typically 1–3 pixels/frame or $\sim 1-3$ km/s). These local poloidal velocities are then averaged over the ~ 20 cm high poloidal range of the box shown in Fig. 2 to get the V_{pol} shown in Fig. 10, which is for a single radial location. The velocity gradient at that radial location is found by making a linear fit to the V_{pol} values in adjacent radial locations over a radial width of $\delta \rho$, where $\delta \rho \sim 1.5$ cm (± 2 pixels) for Figs. 10–12. The results for different radial widths of $\delta \rho \sim 3$ and $\delta \rho \sim 5$ cm are highly correlated with the results for $\delta \rho \sim 1.5$ cm (i.e., R=0.9–0.95), but the relative magnitudes of these slopes decrease from 1 to 0.67 to 0.45 over this range, most likely due to averaging over fine scale structure for higher $\delta \rho$. A comparison of results for $\delta \rho \sim 1.5$ cm and $\delta \rho \sim 5$ cm is shown in Fig. 13.

The V_{pol} determined in this way from cross-correlations functions was compared with the V_{pol} determined from the hybrid optical flow-pattern matching code HOP-V.[43] There was a good cross-correlation coefficient of 0.77 between these two velocity time series for a typical shot, when averaged over the same time interval and poloidal pixel range (± 40 μs and 20 cm). The average velocity using the cross-correlation method was ~ 0.87 times that using HOP-V.[43]

[1]S. M. Kaye, M. G. Bell, R. E. Bell, J. Bialek, T. Bigelow, M. Bitter, P. Bonoli, D. Darrow, P. Efthimion, J. Ferron, E. Fredrickson, D. Gates, L. Grisham, J. Hosea, D. Johnson, R. Kaita, S. Kubota, H. Kugel, B. LeBlanc, R. Maingi, J. Manickam, T. K. Mau, R. J. Maqueda, E. Mazzucato, J. Menard, D. Mueller, B. Nelson, N. Nishino, M. Ono, F. Paoletti, S. Paul, Y.-K. M. Peng, C. K. Phillips, R. Raman, P. Ryan, S. A. Sabbagh, M. Schaffer, C. H. Skinner, D. Stutman, D. Swain, E.

Synakowski, Y. Takase, J. Wilgen, J. R. Wilson, W. Zhu, S. Zweben, A. Bers, M. Carter, B. Deng, C. Domier, E. Doyle, M. Finkenthal, K. Hill, T. Jarboe, S. Jardin, H. Ji, L. Lao, K. C. Lee, N. Luhmann, R. Majeski, S. Medley, H. Park, T. Peebles, R. I. Pinsker, G. Porter, A. Ram, M. Rensink, T. Rognlien, D. Stotler, B. Stratton, G. Taylor, W. Wampler, G. A. Wurden, X. Q. Xu, and L. Zeng, Phys. Plasmas **8**, 1977 (2001).

[2] F. Wagner, Plasma Phys. Controlled Fusion **49**, B1 (2007).

[3] J. W. Connor and H. R. Wilson, Plasma Phys. Controlled Fusion **42**, R1 (2000); T. S. Hahm, *ibid.* **44**, A87 (2002).

[4] F. Wagner, S. Bäumel, J. Baldzuhn, N. Basse, R. Brakel, R. Burhenn, A. Dinklage, D. Dorst, H. Ehmler, M. Endler, V. Erckmann, Y. Feng, F. Gadelmeier, J. Geiger, L. Giannone, P. Grigull, H.-J. Hartfuss, D. Hartmann, D. Hildebrandt, M. Hirsch, E. Holzhauer, Y. Igitkhanov, R. Jänicke, M. Kick, A. Kislyakov, J. Kisslinger, T. Klinger, S. Klose, J. P. Knauer, R. König, G. Kühner, H. P. Laqua, H. Maassberg, K. McCormick, H. Niedermeyer, C. Nührenberg, E. Pasch, N. Ramasubramanian, N. Ruhs, N. Rust, E. Sallander, F. Sardei, M. Schubert, E. Speth, H. Thomsen, F. Volpe, A. Weller, A. Werner, H. Wobig, E. Würsching, M. Zarnstorff, and S. Zoletnik, Phys. Plasmas **12**, 072509 (2005).

[5] R. A. Moyer, K. H. Burrell, T. N. Carlstrom, S. Coda, R. W. Conn, E. J. Doyle, P. Gohil, R. J. Groebner, J. Kim, R. Lehmer, W. A. Peebles, M. Porkolab, C.-L. Rettig, T. L. Rhodes, R. P. Seraydarian R. Stockdale D. M. Thomas, G. R. Tynan, and J. G. Watkins, Phys. Plasmas **2**, 2397 (1995).

[6] T. Ido, Y. Miura, K. Kamiya, Y. Hamada, K. Hoshino, A. Fujisawa, K. Itoh, S.-I. Itoh, A. Nishizawa, H Ogawa, Y. Kusama, and JFT-2M Group, Plasma Phys. Controlled Fusion **48**, S41 (2006); T. Ido, Y. Miura, K. Hoshino, K. Kamiya, Y. Hamada, A. Nishizawa, Y. Kawasumi, H. Ogawa, Y. Nagashima, K. Shinohara, Y. Kusama, and JFT-2M Group, Nucl. Fusion **46**, 512 (2006); K. Ida, Y. Miura, T. Ido, Y. Nagashima, and K. Shinohara, Fusion Sci. Technol. **49**, 122 (2006); T. Ido, K. Kamiya, Y. Miura, Y. Hamada, A. Nishizawa, and Y. Kawasumi, Phys. Rev. Lett. **88**, 055006 (2002).

[7] K. H. Burrell, T. N. Carlstrom, E. J. Doyle, D. Finkenthal, P. Gohil, R. J. Groebner, D. L. Hillis, J. Kim, H. Matsumoto, R. A. Moyer, T. H. Osborne, C. L. Rettig, W. A. Peebles, T. L. Rhodes, H. St. John, R. D. Stambaugh, M. R. Wade, and J. G. Watkins, Plasma Phys. Controlled Fusion **34**, 1859 (1992).

[8] K. H. Burrell, Phys. Plasmas **6**, 4418 (1999).

[9] C. Hidalgo, M. A. Pedrosa, and B. Goncalves, New J. Phys. **4**, 51 (2002).

[10] G. R. Tynan, A. Fujisawa, and G. McKee, Nucl. Fusion **51**, 113001 (2009).

[11] S. J. Zweben, J. A. Boedo, O. Grulke, C. Hidalgo, B. LaBombard, R. J. Maqueda, P. Scarin, and J. Terry, Plasma Phys. Controlled Fusion **49**, S1 (2007).

[12] Y. Andrew, N. C. Hawkes, T. Biewer, K. Crombe1, D. Keeling, E. de la Luna, C. Giroud, A. Korotkov, A. Meigs, A. Murari1, I. Nunes, R. Sartori, T. Tala, and JET-EFDA Contributors, EPL **83**, 15003 (2008).

[13] S.-I. Itoh and K. Itoh, Phys. Rev. Lett. **60**, 2276 (1988).

[14] K. C. Shaing and E. C. Crume, Jr., Phys. Rev. Lett. **63**, 2369 (1989).

[15] A. B. Hassam, T. M. Antonsen, Jr., J. F. Drake, and C. S. Liu, Phys. Rev. Lett. **66**, 309 (1991).

[16] H. Biglari, P. H. Diamond, and P. W. Terry, Phys. Fluids B **2**, 1 (1990).

[17] M. A. Malkov and P. H. Diamond, Phys. Plasmas **15**, 122301 (2008).

[18] K. Miki and P. H. Diamond, Phys. Plasmas **17**, 032309 (2010).

[19] B. Rogers, J. F. Drake, and A. Zeiler, Phys. Rev. Lett. **81**, 4396 (1998).

[20] P. N. Guzdar, R. G. Kleva, R. J. Groebner, and P. Gohil, Phys. Rev. Lett. **89**, 265004 (2002).

[21] X. Xu, R. H. Cohen, W. M. Nevins, G. D. Porter, M. E. Rensink, T. D. Rognlien, J. R. Myra, D. A. D'Ippolito, R. A. Moyer, P. B. Synder, and T. N. Carlstrom, Nucl. Fusion **42**, 21 (2002).

[22] P. H. Diamond, S.-I. Itoh, K. Itoh, and T. S. Hahm, Plasma Phys. Controlled Fusion **47**, R35 (2005).

[23] A. Fujisawa, Nucl. Fusion **49**, 013001 (2009).

[24] G. R. McKee, R. J. Fonck, M. Jakubowski, K. H. Burrell, K. Hallatschek, R. A. Moyer, D. L. Rudakov, W. Nevins, G. D. Porter, P. Schoch, and X. Xu, Phys. Plasmas **10**, 1712 (2003).

[25] A. Krämer-Flecken, S. Soldatov, H. R. Koslowski, O. Zimmermann, and the TEXTOR Team, Phys. Rev. Lett. **97**, 045006 (2006).

[26] A. V. Melnikov, V. A. Vershkov, L. G. Eliseev, S. A. Grashin, A. V. Gudozhnik, L. I. Krupnik, S. E. Lysenko, V. A. Mavrin, S. V. Perfilov, S. A. Shelukhin, S. V. Soldatov, M. C. Ufimtsev, A. O. Urazbaev, G.

Van Oost, and L. G. Zimeleva, Plasma Phys. Controlled Fusion **48**, S87 (2006).

[27] M. G. Shats, H. Xia, and M. Yokoyama, Plasma Phys. Controlled Fusion **48**, S17 (2006).

[28] Y. Hamada, T. Watari, O. Yamagishi, A. Nishizawa, K. Narihara, Y. Kawasumi, T. Ido, M. Kojima, K. Toi, and JIPP T-IIU Group, Phys. Rev. Lett. **99**, 065005 (2007).

[29] G. D. Conway and ASDEX Upgrade Team, Plasma Phys. Controlled Fusion **50**, 085005 (2008).

[30] G. R. McKee, F. Gohil, D. J. Schlossberg, J. A. Boedo, K. H. Burrell, J. S. deGrassie, R. J. Groebner, R. A. Moyer, C. C. Petty, T. L. Rhodes, L. Schmitz, M. W. Shafer, W. M. Solomon, M. Umansky, G. Wang, A. E. White, and X. Xu, Nucl. Fusion **49**, 115016 (2009); D. J. Schlossberg, G. R. McKee, R. J. Fonck, K. H. Burrell, P. Gohil, R. J. Groebner, M. W. Shafer, W. M. Solomon, and G. Wang, Phys. Plasmas **16**, 080701 (2009); D. R. Gupta, R. J. Fonck, G. R. McKee, D. J. Schlossberg, and M. W. Shafer, Phys. Rev. Lett. **97**, 125002 (2006).

[31] G. D. Conway, B. Scott, J. Schirmer, M. Reich, A. Kendl, and ASDEX Upgrade Team, Plasma Phys. Controlled Fusion **47**, 1165 (2005).

[32] M. G. Shats, H. Xia, H. Punzmann, and G. Falkovich, Phys. Rev. Lett. **99**, 164502 (2007).

[33] A. D. Liu, T. Lan, C. X. Yu, H. L. Zhao, L. W. Yan, W. Y. Hong, J. Q. Dong, K. J. Zhao, J. Qian, J. Cheng, X. R. Duan, and Y. Liu, Phys. Rev. Lett. **103**, 095002 (2009).

[34] G. R. Tynan, L. Schmitz, L. Blush, J. A. Boedo, R. W. Conn, R. Doerner, R. Lehmer, R. Moyer, H. Kugel, R. Bell, S. Kaye, M. Okabayashi, S. Sesnic, Y. Sun, and PBX-M Group, Phys. Plasmas **1**, 3301 (1994).

[35] Y. H. Xu, C. X. Yu, J. R. Luo, J. S. Mao, B. H. Liu, J. G. Li, B. N. Wan, and Y. X. Wan, Phys. Rev. Lett. **84**, 3867 (2000).

[36] M. Hirsch, J. Baldzuhn, H. Ehmler, E. Holtzhauer, and F. Wagner, Plasma Phys. Controlled Fusion **48**, S155 (2006).

[37] T. Estrada, T. Happel, L. Eliseev, D. Lopez-Bruna, D. E. Ascasibar, E. Blanco, L. Cupido, J. M. Fontdecaba, C. Hidalgo, R. Jimenez-Gomez, L. Krupnik, M. Liniers, M. E. Manso, K. J. McCarthy, F. Medina, A. Melnikov, B. van Milligen, M. A. Ochando, I. Pastor, M. A. Pedrosa, F. L. Tabares, and D. Tafalla, Plasma Phys. Controlled Fusion **51**, 124015 (2009).

[38] S. J. Zweben, R. J. Maqueda, J. L. Terry, J. R. Myra, D. D'Ippolito, D. A. Russell, J. A. Krommes, B. LeBlanc, T. Stoltfus-Dueck, D. P. Stotler, K. M. Williams, C. E. Bush, R. Maingi, O. Grulke, S. A. Sabbagh, and A. E. White, Phys. Plasmas **13**, 056114 (2006).

[39] A. E. White, S. J. Zweben, M. J. Burin, T. A. Carter, T. S. Hahm, J. A. Krommes, and R. J. Maqueda, Phys. Plasmas **13**, 072301 (2006).

[40] S. J. Zweben, R. J. Maqueda, D. P. Stotler, A. Keesee, J. Boedo, C. E. Bush, S. M. Kaye, B. LeBlanc, J. L. Lowrance, V. J. Mastrocola, R. Maingi, N. Nishino, G. Renda, D. W. Swain, J. B. Wilgen, and NSTX Team, Nucl. Fusion **44**, 134 (2004).

[41] R. J. Maqueda, G. A. Wurden, D. P. Stotler, S. J. Zweben, B. LaBombard, J. L. Terry, J. L. Lowrance, V. J. Mastrocola, G. F. Renda, D. A. D'Ippolito, and J. R. Myra, Rev. Sci. Instrum. **74**, 2020 (2003); R. J. Maqueda, D. P. Stotler, and NSTX Team, Nucl. Fusion **50**, 075002 (2010).

[42] D. P. Stotler, B. LaBombard, J. L. Terry, and S. J. Zweben, J. Nucl. Mater. **313–316**, 1066 (2003).

[43] T. Munsat and S. J. Zweben, Rev. Sci. Instrum. **77**, 103501 (2006); Y. Sechrest and T. Munsat, private communication (2010).

[44] R. Sánchez, B. Ph. van Milligen, D. E. Newman, and B. E. Carreras, Phys. Rev. Lett. **90**, 185005 (2003); V. E. Lynch, B. A. Carreras, R. Sanchez, B. LaBombard, B. Ph. van Mulligan, and D. E. Newman, Phys. Plasmas **12**, 052304 (2005).

[45] Y. Xu, S. Jachmich, R. R. Weynants, M. Van Schoor, M. Vergote, A. Kramer-Flecken, O. Schmitz, B. Unterberg, C. Hidalgo, and TEXTOR Team, Phys. Plasmas **16**, 110704 (2009); J. A. Boedo, D. S. Gray, P. W. Terry, S. Jachmich, G. R. Tynan, R. W. Conn, and TEXTOR-94 Team, Nucl. Fusion **42**, 117 (2002); T. Carter and J. E. Maggs, Phys. Plasmas **16**, 012304 (2009).

[46] K. Hallatschek and A. Zeiler, Phys. Plasmas **7**, 2554 (2000).

[47] D. A. Russell, J. R. Myra, and D. A. D'Ippolito, Phys. Plasmas **16**, 122304 (2009).

[48] A. Bencze, M. Berta, S. Zoletnik, J. Stockel, J. Adamek, and M. Hron, Plasma Phys. Controlled Fusion **48**, S137 (2006).